



# Pac1/LIS1 stabilizes an uninhibited conformation of dynein to coordinate its localization and activity

Matthew G. Marzo, Jacqueline M. Griswold and Steven M. Markus  

**Dynein is a microtubule motor that transports many different cargos in various cell types and contexts. How dynein is regulated to perform these activities with spatial and temporal precision remains unclear. Human dynein is regulated by autoinhibition, whereby intermolecular contacts limit motor activity. Whether this mechanism is conserved throughout evolution, whether it can be affected by extrinsic factors, and its role in regulating dynein function remain unclear. Here, we use a combination of negative stain electron microscopy, single-molecule assays, genetic, and cell biological techniques to show that autoinhibition is conserved in budding yeast, and plays a key role in coordinating in vivo dynein function. Moreover, we find that the Lissencephaly-related protein, LIS1 (Pac1 in yeast), plays an important role in regulating dynein autoinhibition. Our studies demonstrate that, rather than inhibiting dynein motility, Pac1/LIS1 promotes dynein activity by stabilizing the uninhibited conformation, which ensures appropriate dynein localization and activity in cells.**

Cytoplasmic dynein relies on a complex network of regulators to support its many functions. For example, processive motility of human dynein requires the dynactin complex and an adapter that links them together<sup>1,2</sup>. The reliance on cargo-specific adapters (such as BicD2 and Hook3)<sup>1,2</sup> ensures that dynein and dynactin are linked together at the right time and place for appropriate motility. Dynactin supports dynein motility by promoting microtubule binding<sup>3</sup> and by orienting the motor domains in a parallel manner that is conducive for motility<sup>4</sup>. In addition to its regulation by extrinsic factors, studies have shown that human dynein-1 and dynein-2 are autoregulated by intracomplex interactions. Specifically, intermolecular interactions between the motor domains stabilize an autoinhibited conformation of human dynein called the phi particle (named due to its resemblance to the Greek character)<sup>4–7</sup>. For dynein-2 (which is responsible for intraflagellar transport), the autoinhibited conformation—which has been observed in its native context<sup>7</sup>—reduces its velocity, ATPase activity and microtubule landing rate<sup>6</sup>. Similarly, the autoinhibited dynein-1 conformation has been shown to reduce its microtubule landing rate and motility properties<sup>4,8</sup>. Autoinhibition of dynein-1 also prevents its interaction with dynactin and BicD2 (ref. <sup>4</sup>).

Although it is well established that human dynein adopts the autoinhibited conformation, the extent of its evolutionary conservation is unclear. Yeast dynein is of particular interest owing to two notable in vitro discrepancies with human dynein: (1) yeast dynein is processive in single-molecule assays without the need for other factors, such as dynactin<sup>9</sup>; and (2) yeast dynein has been reported to interact with dynactin in the absence of adapters<sup>10</sup>. The reasons for these differences are unclear, but one possibility is that yeast dynein does not adopt the autoinhibited conformation, which could potentially account for its ability to walk in the absence of dynactin. This is supported by studies showing that artificially separating the motor domains of human dynein-1 with a rigid linker (and, therefore, preventing intermolecular contacts) is sufficient to convert it to a processive motor<sup>8</sup>.

Another important effector of dynein activity is the lissencephaly protein LIS1, which is required for numerous dynein functions in cells<sup>11–13</sup>, including promoting dynein recruitment to cellular sites<sup>14,15</sup> and assisting in dynein transport functions, including nuclear migration

in neurons<sup>16,17</sup>, and high-load vesicular transport<sup>18–21</sup>. However, the mechanism by which LIS1 affects dynein activity remains controversial. For example, in vitro studies have shown that LIS1 reduces the velocity of dynein alone<sup>21–23</sup>, but increases the velocity of dynein–dynactin–BicD2 (refs. <sup>23,24</sup>). In addition to promoting dynein force production<sup>21</sup>, studies have shown that LIS1 promotes initiation of dynein–dynactin–BicD2 motility from the plus ends of dynamic microtubules<sup>23,25</sup>. Studies with the budding yeast homologue of LIS1, Pac1, have shown that Pac1 reduces the velocity of dynein motility<sup>26–29</sup>, presumably by uncoupling the ATPase cycle from the conformational changes in the motor and microtubule-binding domains (MTBDs) that elicit microtubule release<sup>27,28</sup>. Thus, the precise role for Pac1/LIS1 in dynein function remains confounded by these contrasting results. Although a role for Pac1/LIS1 in regulating the autoinhibited conformation has not yet been reported, two studies found that LIS1 can indeed promote dynein–dynactin interaction<sup>30,31</sup>, which is an expected consequence of relieving dynein autoinhibition<sup>4</sup>.

We set out to address the question of whether yeast dynein adopts an autoinhibited conformation and, if so, what role it has in regulating dynein activity. Our recent findings suggested that yeast dynein indeed adopts such a conformation<sup>32</sup>. Specifically, we found that engineering a neurological disease-correlated mutation into yeast dynein leads to increased run lengths of single molecules of dynein, and a localization pattern in cells that is indicative of an enhanced dynein–dynactin interaction. This mutation was at a residue that was recently shown to be important for maintenance of the autoinhibited conformation of human dynein<sup>4</sup>. Here we used a combination of in vitro and in vivo approaches to show that yeast dynein indeed adopts an autoinhibited conformation that restricts its in vitro processivity, and coordinates its localization and activity in cells. Moreover, we found that Pac1 is an important effector of this conformational state—rather than inhibiting dynein motility, Pac1 promotes its activity by stabilizing the uninhibited conformation.

## Results

**Yeast dynein adopts an autoinhibited phi-particle conformation.** To determine whether yeast dynein adopts an autoinhibited conformation<sup>5</sup>, we developed a strategy to isolate biochemical

quantities of the intact yeast dynein complex to a high degree of purity. The yeast dynein complex is comprised of light (Dyn2), light-intermediate (Dyn3), intermediate (Pac11) and heavy chains (Dyn1)<sup>33</sup>, the latter of which is the catalytic subunit responsible for motility. We generated a polycistronic plasmid containing all of the dynein complex subunits each under the control of the galactose-inducible promoter (*GAL1p*). We included a tandem affinity tag (8His-ZZ (HZZ)) followed by either a SNAP or HALO tag on the N terminus of Dyn1 for purification and fluorescence labelling of the complex, respectively (Fig. 1a). Single-molecule motility assays with the purified complex confirmed its activity was nearly identical to the non-overexpressed complex (Fig. 1b; see below). The increased yield enabled us to isolate the complex to a high degree of purity using size exclusion chromatography, which revealed an elution profile that was nearly identical to the recombinant human dynein complex (Fig. 1c).

We used negative stain electron microscopy (EM) to obtain the first high-magnification view of the intact yeast dynein complex. This revealed the presence of dynein complexes in both an open uninhibited state and those in an apparent autoinhibited conformation, with the large majority being in the autoinhibited state (Extended Data Fig. 1). Class averages appeared to be strikingly similar to the intact human dynein-1 complex<sup>1,4</sup>, as well as to an artificially dimerized motor domain truncation of dynein-2 in the autoinhibited conformation<sup>6</sup> (Fig. 1d). The N-terminal tail domains—which exhibit flexibility with respect to the motor domains—appear twisted around one another in two-dimensional (2D) and 3D averages (Fig. 1e, Supplementary Video 1). Intermolecular contacts appear to extend to the motor domains and the coiled-coil stalks (the latter of which cross in an X-like configuration), which connect the AAA rings to the MTBDs. We confirmed a high degree of similarity between the human and yeast dynein phi particles by manually docking a high-resolution structure of human dynein<sup>4</sup> into our 3D model (Fig. 1e, Supplementary Video 1).

Previous observations of an artificially dimerized, truncated yeast dynein motor domain fragment (lacking the N-terminal tails) revealed no phi particles (as noted by negative stain EM<sup>26</sup>, and within the crystal lattice<sup>34,35</sup>). Thus, in contrast to human dynein-2, for which the motor domain is sufficient to form the phi particle<sup>6,36</sup>, yeast dynein requires the tail to do so. We also noted several class averages that showed conformations in which the motor domains are closely apposed but unbound, and the tails are wrapped around one another (Fig. 1d; classes vii and viii), indicating that intermolecular contacts within the tails can stabilize motor domain-independent tail–tail interactions. This also suggests that the transition to the autoinhibited conformation may be initiated by tail–tail contacts, which seem to be required to stabilize the motor domains in the autoinhibited conformation.

**The autoinhibited conformation restricts in vitro processivity.** To determine whether the increased processivity that we previously

noted for the neurological disease-correlated K1475Q mutation<sup>32</sup> is a consequence of disrupted phi particle formation, we sought to assess the consequences of mutating other intermolecular surfaces. The human dynein phi-particle structure identified four key intermolecular surfaces<sup>4</sup> (Fig. 2a). Sequence alignment and homology modelling of Dyn1 into this structure revealed a high degree of conservation at all four surfaces (Fig. 2a). We found that increasing degrees of disruption of a predicted tripartite salt bridge at surface 2 increased processivity in a stepwise manner that we were able to reduce by repairing the broken electrostatic pairing (Fig. 2b). Consistent with the apparent stalk–stalk contact (Fig. 1d, classes i–v), we noted a large increase in run length for surface 3 mutants. In contrast to surface 2 mutants, surface 3 mutants moved slower; this may be due to disrupted kinetics of helix sliding in the coiled-coil stalk, which is responsible for communicating nucleotide-dependent conformational changes within the motor domain to the MTBD<sup>36–39</sup>. Processivity also increased for surface 4 mutants, with one of them reducing velocity to ~50% that of the wild type. Finally, fluorescence intensity measurements confirmed that the run-length increases for the most processive mutants (D2868K and I3272A) are not a consequence of protein aggregation (Extended Data Fig. 2a–c). These results indicate that the three surfaces tested here are important for forming the autoinhibited conformation of yeast dynein, which limits its in vitro processivity (Supplementary Video 3).

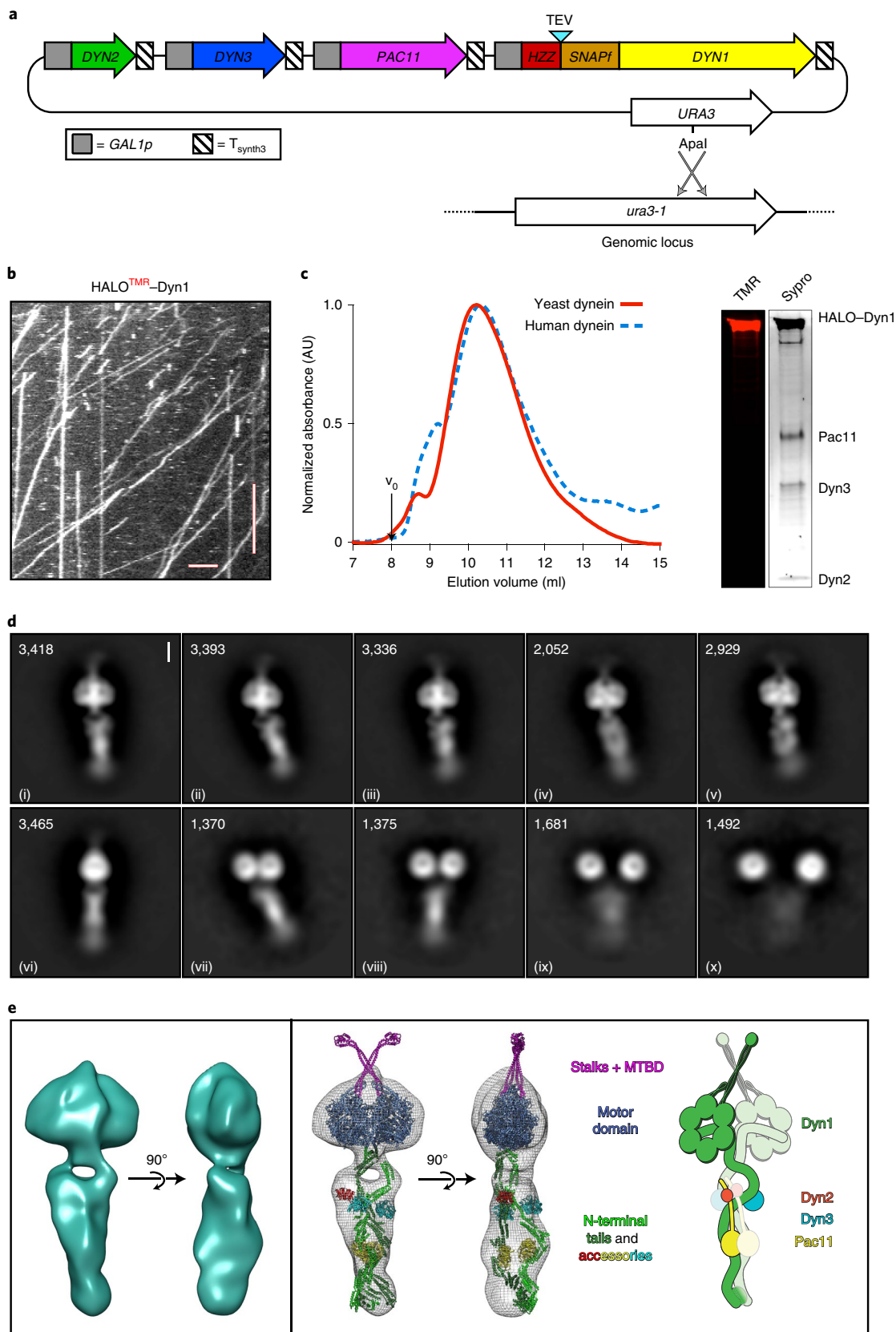
As noted above, the GST-dimerized yeast dynein motor domain (GST–dynein<sup>MOTOR</sup>, Extended Data Fig. 3b) likely does not adopt the autoinhibited conformation. Consistent with this notion, GST–dynein<sup>MOTOR</sup> with D2868K did not exhibit increased processivity (Extended Data Fig. 3), further indicating that the reason for the increased run lengths for full-length dynein is disruption of the autoinhibited conformation, and not altered mechanochemistry. It is interesting to note that GST–dynein<sup>MOTOR</sup> exhibits run-lengths (1.1–1.6  $\mu$ m; Extended Data Figs. 3 and 7f) that are much lower than the run-lengths of the uninhibited dynein mutants ( $\leq 7.2 \mu$ m, or 4.5-fold higher), despite this fragment not adopting the autoinhibited conformation. This indicates that the tail domain permits a motor domain arrangement that is more conducive to processive motility than the GST, which is consistent with the higher force generation capacity<sup>40</sup> of the intact dynein complex compared with GST–dynein<sup>MOTOR</sup>.

Although disruption of the human dynein phi particle increases its microtubule association<sup>4</sup>, we observed only a small increase in the landing rate of the uninhibited mutant (Extended Data Fig. 4a). We noted a similarly small increase in the microtubule affinity of the uninhibited mutant using a microtubule cosedimentation assay (Extended Data Fig. 4b,c). Although the reason that uninhibited yeast dynein does not exhibit increased microtubule-binding affinity is unclear, our findings indicate that microtubule association of wild-type yeast dynein is likely not restricted by the autoinhibited conformation.

**Fig. 1 | The yeast dynein complex adopts an autoinhibited phi-particle conformation.** **a**, Schematic of the polycistronic plasmid that we used to produce the intact yeast dynein complex (*GAL1p*, galactose-inducible promoter; *T<sub>synth3r</sub>*, terminator sequence<sup>56</sup>). Restriction digest with *Apal* (cuts within *URA3*) targets the plasmid for homologous recombination into the *ura3-1* locus, as shown. **b**, Representative kymograph showing single-molecule motility of the purified overexpressed yeast dynein complex. Scale bars, 4  $\mu$ m (horizontal) and 2 min (vertical). **c**, Representative elution profiles of yeast and human dynein complexes from Superose 6 resin (left), and scans of the same polyacrylamide gel depicting fluorescently labelled Dyn1 (using HaloTag–TMR) and the entire complex (using Sypro Ruby staining; right); three independent preparations yielded very similar results. **d**, Representative negative stain EM class averages of the intact yeast dynein complex (2D classes were generated from one preparation; however, independent preparations provided very similar raw images). Scale bar, 10 nm. The number of particles used to generate each class is indicated in each panel. Classes i–vi show dynein in the autoinhibited phi-particle conformation, whereas classes vii–x show dynein in various open, uninhibited states. **e**, 3D models of dynein in the autoinhibited state generated from 2D class averages with (right) and without (left) a high-resolution 3D structure of human dynein-1 in the phi-particle conformation (PDB 5NVU<sup>4</sup>) manually docked into it. Note that the atomic structures of the two tail domains have been slightly rotated with respect to the motor domains to better fit the 3D model, and that the structures of both TcTEX and Rob1 have been eliminated owing to their absence from the yeast dynein complex (Extended Data Fig. 1, Supplementary Video 1).

**Dynein autoinhibition restricts cortical localization and dynactin association.** Although uninhibited human dynein mutants exhibited unchanged processivity, they were noted to have higher affinity for dynactin and BicD2 (ref. <sup>4</sup>). In yeast, dynein-mediated

recruitment of dynactin to microtubule plus ends is required for their localization to cortical Num1 receptor sites<sup>41,42</sup> (Fig. 3a). Thus, uninhibited dynein mutant cells would be expected to show enhanced dynactin recruitment to plus ends, and an increased



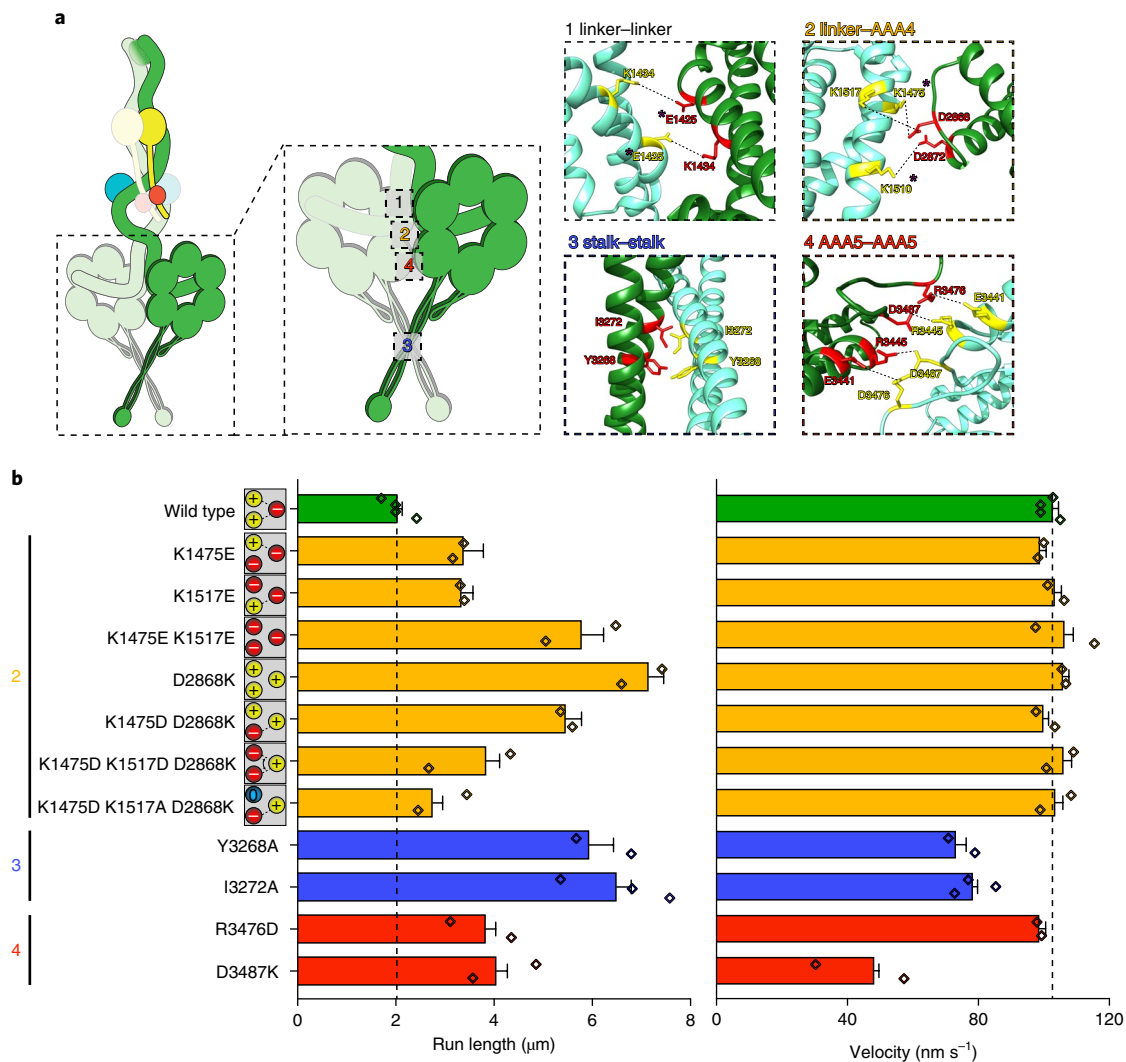


**Fig. 2 | Disrupting phi-particle contact points extends single-molecule run lengths.** **a**, Cartoon depicting four predicted intermolecular contact surfaces within the motor domains that stabilize the phi-particle conformation. Insets: regions of yeast dynein modelled into the human dynein phi-particle structure. Structural models were generated using one-to-one threading of the yeast *DYN1* sequence into PDB 5NVU<sup>4</sup> on the Phyre2 server<sup>57</sup>. Residues indicated by magenta asterisks are mutated in patients with neurological disease<sup>58–60</sup>, suggesting that autoinhibition is critical for normal cellular dynein function. **b**, Single-molecule run-length and velocity values for wild-type and mutant dyneins with phi-particle-disrupting mutations (at surfaces 2, 3 and 4, as indicated). The cartoons along the vertical axis show electrostatic interactions (or lack thereof) among residues 1517, 1475 (left circles) and 2868 (right circle) at the linker-AAA4 surface. Note that the degree of processivity enhancement is inversely proportional to the number of charge interactions at this surface. The diamonds represent mean values obtained from each independent replicate experiment; from top to bottom,  $n=528$  (4),  $n=400$  (2),  $n=361$  (2),  $n=213$  (2),  $n=409$  (2),  $n=352$  (2),  $n=233$  (2),  $n=323$  (2),  $n=170$  (2),  $n=462$  (3),  $n=362$  (2) and  $n=319$  (2) motors (independent replicates). The error bars show the s.e. Note that we generated and tested the motility of two other point mutants at interface 4—E3441K and R3445D—both of which were inactive in single-molecule assays (not shown) (Extended Data Figs. 2, 3 and 4, Supplementary Video 3).

frequency of dynein cortical localization. As expected, cortical dynein foci were more frequently observed in mutant cells in a manner that required dynactin (Fig. 3b,c). The *dyn1*<sup>D2868K</sup> cells also had a greater frequency of spindle pole body-associated dynein foci (that is, at the minus ends), where active dyneins were shown to accumulate<sup>43</sup>. Finally, ratiometric fluorescence intensity measurements revealed a significant increase in the relative ratio of dynactin to dynein at microtubule plus ends in the D2868K mutant (1.06 to 1.45;  $P=0.0012$ ; Fig. 3d,e).

**Peptide insertion between motor and tail domains ablates the autoinhibited conformation.** We noted that the uninhibited mutants also localized more frequently to plus ends (Fig. 3b), a pattern that is similar to the pattern of a truncated dynein

motor fragment (dynein<sup>MOTOR</sup>)<sup>42</sup> and a dynein mutant with a helical linker peptide (helical linker 3 (HL3)) inserted between the tail and motor domains<sup>29</sup> (dynein<sup>HL3</sup>; Fig. 4a). Notably, dynein<sup>HL3</sup> also localizes to the cell cortex more frequently than wild type<sup>29</sup>, much like a tail domain fragment<sup>42</sup>. We originally generated the dynein<sup>HL3</sup> mutant<sup>29</sup> to test the hypothesis<sup>42</sup> that the motor domain restricts the Num1-binding capacity of the dynein tail. We predicted that the HL3 peptide would sufficiently separate the tail and motor domains such that the motor domain would no longer have this ability (that is, would ‘unmask’ the tail domain; Fig. 4a, original model). Although localization data<sup>29</sup> supported this hypothesis, there has been no additional evidence that favours this mechanism. We questioned whether HL3 simply disrupts the autoinhibited conformation (Fig. 4a, revised model), which



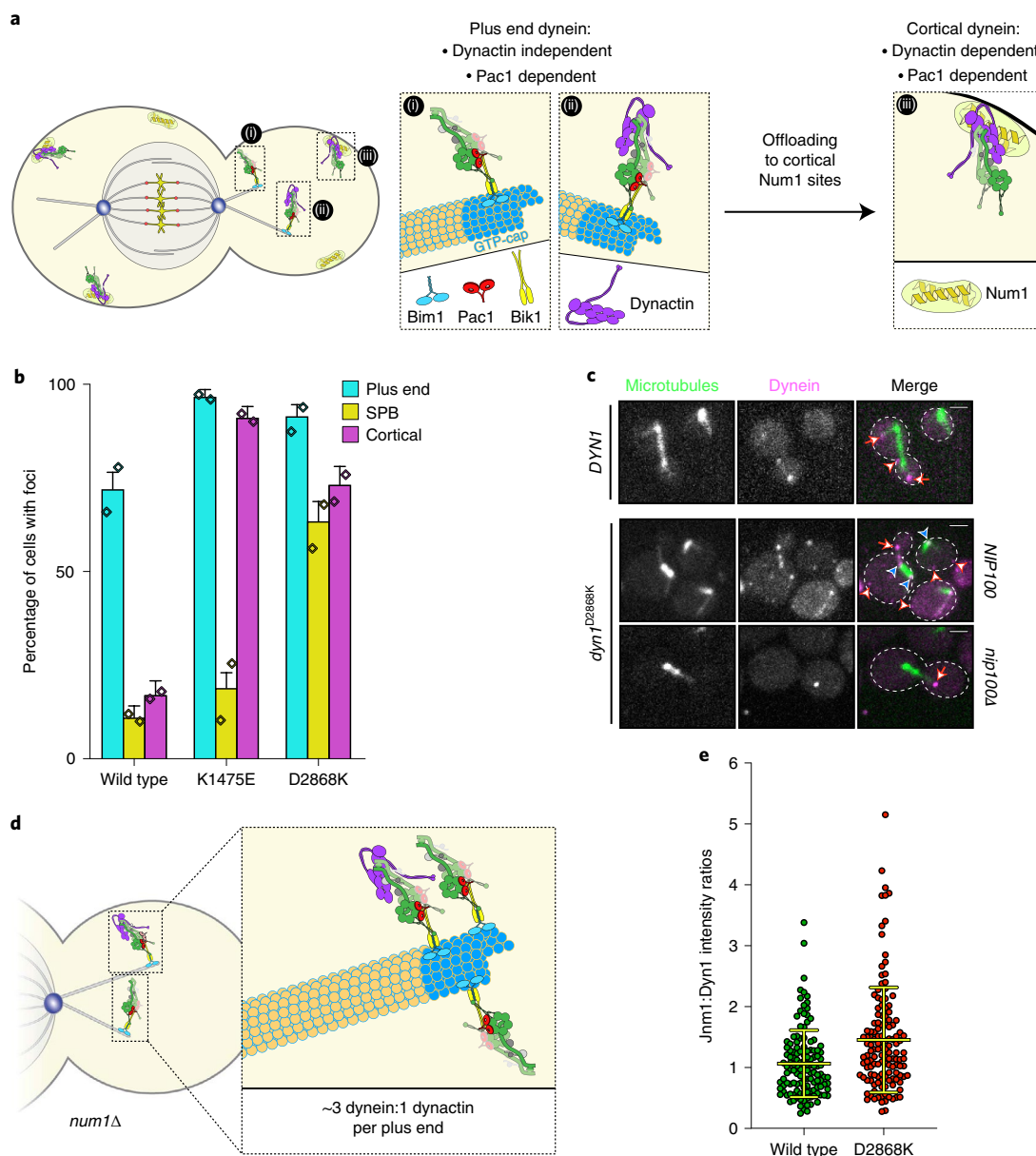


**Fig. 3 | The autoinhibited conformation restricts cellular localization of dynein and its interaction with dynactin.** **a**, Cartoon depicting the two main sites of dynein localization (microtubule plus ends and cell cortex), and the molecular requirements for each. Dynein plus end localization (i) requires Bik1 (ref. <sup>50</sup>) and Pac1 (ref. <sup>44</sup>) with Bim1 potentially playing some role in this process, but does not require dynactin<sup>41</sup>. Rather, dynactin plus end localization (ii) is dependent on dynein<sup>41</sup>. Subsequent to plus end targeting, dynein-dynactin complexes are offloaded to cortical Num1 sites<sup>29,61</sup> (iii). **b**, The fraction of cells (weighted mean) with the indicated mutant or wild-type Dyn1-3GFP foci;  $n = 100$ ,  $n = 90$  and  $n = 82$  mitotic cells from two independent experiments. The error bars indicate weighted s.e. of proportion; the diamonds represent mean values obtained from each independent replicate experiment. **c**, Representative images of wild-type or mutant dynein (D2868K) localizing in otherwise wild-type (*NIP100*) or *nip100Δ* (dynactin component) cells. Note the lack of cortical localization of dynein<sup>D2868K</sup> in *nip100Δ* cells. The white arrowheads indicate cortical foci, the white arrows indicate plus end foci and the blue arrowheads indicate spindle pole body (SPB) foci. Similar results were obtained from two independent replicates. Scale bars, 2  $\mu$ m. **d**, Cartoon depicting the relative ratio of dynein to dynactin at microtubule plus ends (~3 dynein:1 dynactin), on the basis of previous quantitative ratiometric imaging<sup>49</sup>. **e**, Scatter plot (data are mean  $\pm$  s.d.) of the ratios of fluorescence intensity values for Jnm1-3mCherry (dynactin component p50/dynamitin):Dyn1-3GFP at individual microtubule plus ends and SPBs;  $n = 132$  (left) and  $n = 145$  (right) plus ends or SPBs, from two independent experiments. Background-corrected intensity values of colocalizing Jnm1-3mCherry and Dyn1-3GFP foci were each divided to obtain individual ratio values. Measurements were taken from *num1Δ* cells to prevent offloading of assembled dynein-dynactin complexes from plus ends.

would result in an enhanced interaction between dynein, dynactin and Num1.

Single-molecule analysis of dynein<sup>HL3</sup> revealed that this mutant exhibits longer run-lengths than dynein<sup>D2868K</sup> (Fig. 4b; both produced as shown in Fig. 1a) and velocities similar to GST-dynein<sup>MOTOR</sup>

(Extended Data Fig. 3c), suggesting that HL3 indeed disrupts autoinhibition. We noted that the overexpressed wild-type dynein complex exhibited slightly longer runs than the non-overexpressed complex (2.3  $\mu$ m versus 2.0  $\mu$ m;  $P = 0.0049$ ). This is likely due to a subset of the motors aggregating, as apparent from the presence

of a small fraction of particles with higher fluorescence intensities (Extended Data Fig. 2d). Importantly, aggregation cannot account for the increased processivity of dynein<sup>HL3</sup> (Extended Data Fig. 2e,f).

We previously noted that, similar to dynein<sup>MOTOR</sup>, dynein<sup>HL3</sup> exhibits higher affinity for Pac1 (LIS1 homologue) than wild-type dynein<sup>9,29,42</sup>. We questioned whether this is a consequence of disrupted autoinhibition. Using a copelleting assay, we found that Pac1 indeed preferentially binds to dynein<sup>D2868K</sup>, dynein<sup>HL3</sup> and GST–dynein<sup>MOTOR</sup> (Fig. 4c). This also indicates that the likely reason for the altered localization<sup>29</sup> and single-molecule behaviour of dynein<sup>HL3</sup> is that it is in a constitutively uninhibited state.

**Disruption of autoinhibition permits Pac1-independent cellular dynein activity.** Given the similarities between the uninhibited mutants and dynein<sup>HL3</sup>, we wondered whether the Pac1-independent cortical localization of dynein<sup>HL3</sup> is also a consequence of uninhibition<sup>29</sup>. Pac1 is required for normal plus end and cortical localization of wild-type dynein<sup>42,44</sup> (Fig. 4d), which is consistent with the offloading model for dynein function, in which dynein is offloaded from the plus ends to cortical Num1 sites<sup>29</sup>. However, dynein<sup>K1475E</sup> and dynein<sup>D2868K</sup> were found at the cortex in *pac1Δ* cells (Fig. 4d). We also found that the uninhibited mutants partly rescued *pac1Δ*-dependent synthetic growth defects with *kar9Δ* (which effects a parallel mechanism of spindle orientation<sup>45–47</sup>), suggesting that the uninhibited dynein mutants can compensate in part for the loss of Pac1 (Fig. 4e, Extended Data Fig. 5a,b). We did not observe a similar rescue for cells expressing dynein<sup>HL3</sup> (Extended Data Fig. 5c), suggesting that, although this mutant bypasses Pac1 for cortical localization<sup>29</sup> and is highly processive in vitro, it is unable to move the spindle in cells.

As expected, we observed almost no dynein-mediated spindle movements in *pac1Δ* cells expressing either wild type or dynein<sup>HL3</sup> (Fig. 4f,g). However, we did observe dynein-mediated spindle movements in *pac1Δ* cells expressing either dynein<sup>K1475E</sup> or dynein<sup>D2868K</sup>, indicating that the Pac1-independent cortical populations of these mutants are active (Fig. 4f,g, Supplementary Video 2). Given the ability of the uninhibited dynein mutants to rescue loss of Pac1, this suggests that one function of Pac1 is to relieve dynein autoinhibition.

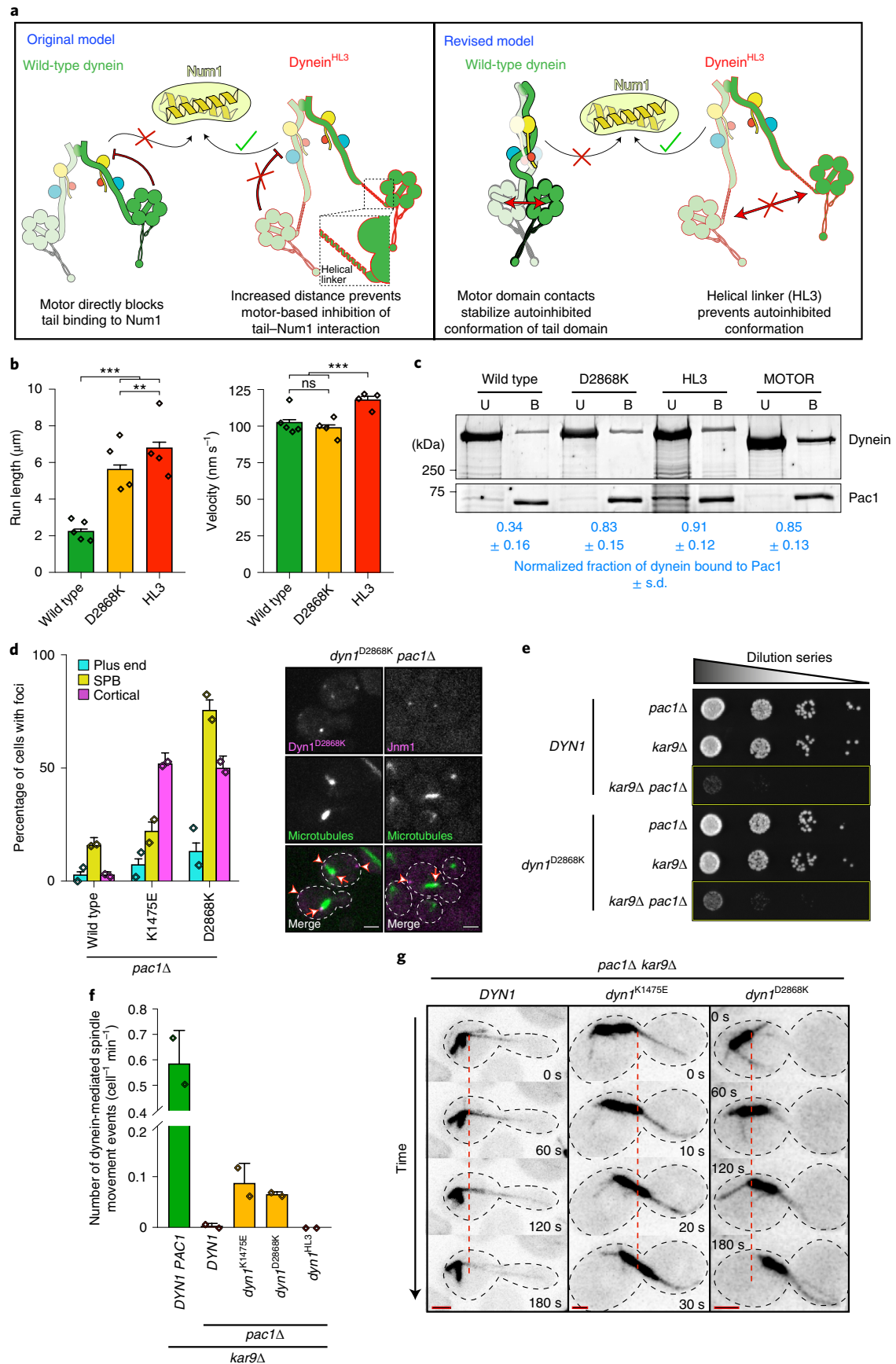
**Pac1 stabilizes the uninhibited conformation of motile dynein complexes.** To gain additional insight into the potential mechanism by which Pac1 may be affecting dynein autoinhibition, we studied the available structures. Docking of a Pac1-bound motor domain structure<sup>28</sup> into one of the two motors in the autoinhibited state<sup>4</sup> revealed an apparent clash between Pac1 and the motor domain to

which Pac1 is not bound (Fig. 5a), suggesting that, when Pac1 is bound to dynein, the autoinhibited conformation is sterically precluded. This accounts for the enhanced affinity of Pac1 for the uninhibited mutants, and also for dynein<sup>MOTOR</sup>.

To test whether Pac1 could affect dynein autoinhibition, we sought to reassess the effect of Pac1 on dynein motility. We predicted that if Pac1 prevents autoinhibition, then it would increase dynein processivity. Studies that described the effect of Pac1 on dynein<sup>26,27,29</sup> contrast with recent studies using human LIS1 (refs. <sup>23–25</sup>). Whereas Pac1 reduces dynein velocity and promotes a microtubule-bound state<sup>26–28</sup>, LIS1 either increases the velocity of human dynein–dynactin complexes<sup>23,24</sup> or has no effect on velocity<sup>25</sup>. In these latter studies, LIS1 was observed comigrating with dynein–dynactin at varying degrees. Thus, to clearly define how Pac1 affects dynein, we sought to assess comigrating dynein–Pac1 complexes. However, we noted that even at nanomolar concentrations, Pac1 bound extensively along microtubules in our motility buffer (Extended Data Fig. 6a). This is in stark contrast to LIS1, which does not bind to microtubules, as assessed by various means<sup>21,23–25</sup>. We found that the Pac1–microtubule interaction was sensitive to ionic strength—Pac1 strongly binds to microtubules in buffer supplemented with 50 mM potassium acetate (conditions that have previously been used to assess the effect of Pac1 on dynein<sup>26,29</sup>), but binds to a much lesser extent in 150 mM potassium acetate (161.5 mM ionic strength; Extended Data Fig. 6a,b). We also found that Pac1 binding to microtubules requires the tubulin C-terminal tails (Extended Data Fig. 6c), and can be reduced by the presence of other cellular factors (through the addition of cellular extracts; Extended Data Fig. 6d,e). To clearly assess the effect of Pac1 on dynein motility, we therefore used conditions in which Pac1–microtubule binding is strongly reduced (Fig. 5b).

Two-colour imaging of dynein preincubated with Pac1 revealed many examples of their comigration (Fig. 5c,e). We noted that comigrating dynein–Pac1 complexes (Fig. 5d, magenta bars) moved with significantly longer run lengths than those dyneins not comigrating with Pac1 in the same imaging chamber (yellow bars), and than those dyneins that were not preincubated with Pac1 (green bars). Fluorescence intensity analysis revealed that the increased dynein–Pac1 run lengths were not a consequence of dynein aggregation (Extended Data Fig. 2e,g). Consistent with the enhanced affinity of Pac1 for the uninhibited mutants, we observed a greater frequency of Pac1 comigrating with dynein<sup>D2868K</sup> and dynein<sup>HL3</sup> than with wild-type dynein (Fig. 5e). However, we noted only a small (D2868K) or no (HL3) Pac1-dependent run-length increase for either of these mutants, further supporting the notion that they are already uninhibited and are therefore refractory to Pac1 activity. These data

**Fig. 4 | Preventing dynein autoinhibition enables Pac1/LIS1-independent localization and function.** **a**, Models accounting for dynein<sup>HL3</sup> phenotypes<sup>29</sup>. The tail domain of full-length, wild-type dynein cannot associate with Num1 in the absence of plus end-targeting; however, the addition of HL3 between the tail and motor domains enables plus end-targeting-independent dynein–Num1 interaction<sup>29</sup>. Our original model posited that this was due to the motor precluding the tail–Num1 interaction. Our revised model posits that motor domain contacts stabilize the autoinhibited conformation, in which the tail domains adopt a twisted state that is unable to interact with Num1. We propose that HL3 insertion prevents adoption of the autoinhibited conformation. **b**, Motility assay parameters, measured from single molecules of motors purified using the strategy described in Fig. 1a; from left to right,  $n = 840$  (5),  $n = 586$  (4) and  $n = 642$  (4) motors (independent replicates). The error bars indicate s.e.; ns,  $P = 0.1563$ ; \*\* $P = 0.0092$ ; \*\*\* $P < 0.0001$ . The diamonds indicate mean values obtained from independent replicates. **c**, Binding assay illustrating increased affinity of Pac1 for uninhibited dyneins (see Methods). The values represent the mean corrected band intensities; from left to right,  $n = 3$ ,  $n = 3$ ,  $n = 2$  and  $n = 3$  independent experiments. **d**, The fraction of cells (weighted mean) with mutant or wild-type Dyn1–3GFP foci in *pac1Δ* cells (left); from left to right,  $n = 113$ ,  $n = 108$  and  $n = 90$  mitotic cells from two independent experiments. The error bars indicate weighted s.e. of proportion and the diamonds represent mean values obtained from independent replicates. Right, representative images showing the presence of cortical dynein and dynactin (Jnm1) foci in *dyn<sup>D2868K</sup> pac1Δ* cells. The arrowheads indicate cortical foci and the arrows indicate SPB foci. Scale bars, 2  $\mu$ m. **e**, Serial dilutions of cells with the indicated genotype (note differences in cell growth in yellow boxes). A representative assay is shown; similar results were obtained from two independent replicates. **f,g**, Relative in vivo dynein activity (**f**) with representative time-lapse images (**g**; see Methods);  $n = 35$ ,  $n = 30$ ,  $n = 30$ ,  $n = 30$  and  $n = 32$  cells from two independent experiments. The diamonds indicate mean values obtained from independent replicates. Scale bars, 2  $\mu$ m. The dashed lines provide a point of reference (Extended Data Fig. 5, Supplementary Video 2).



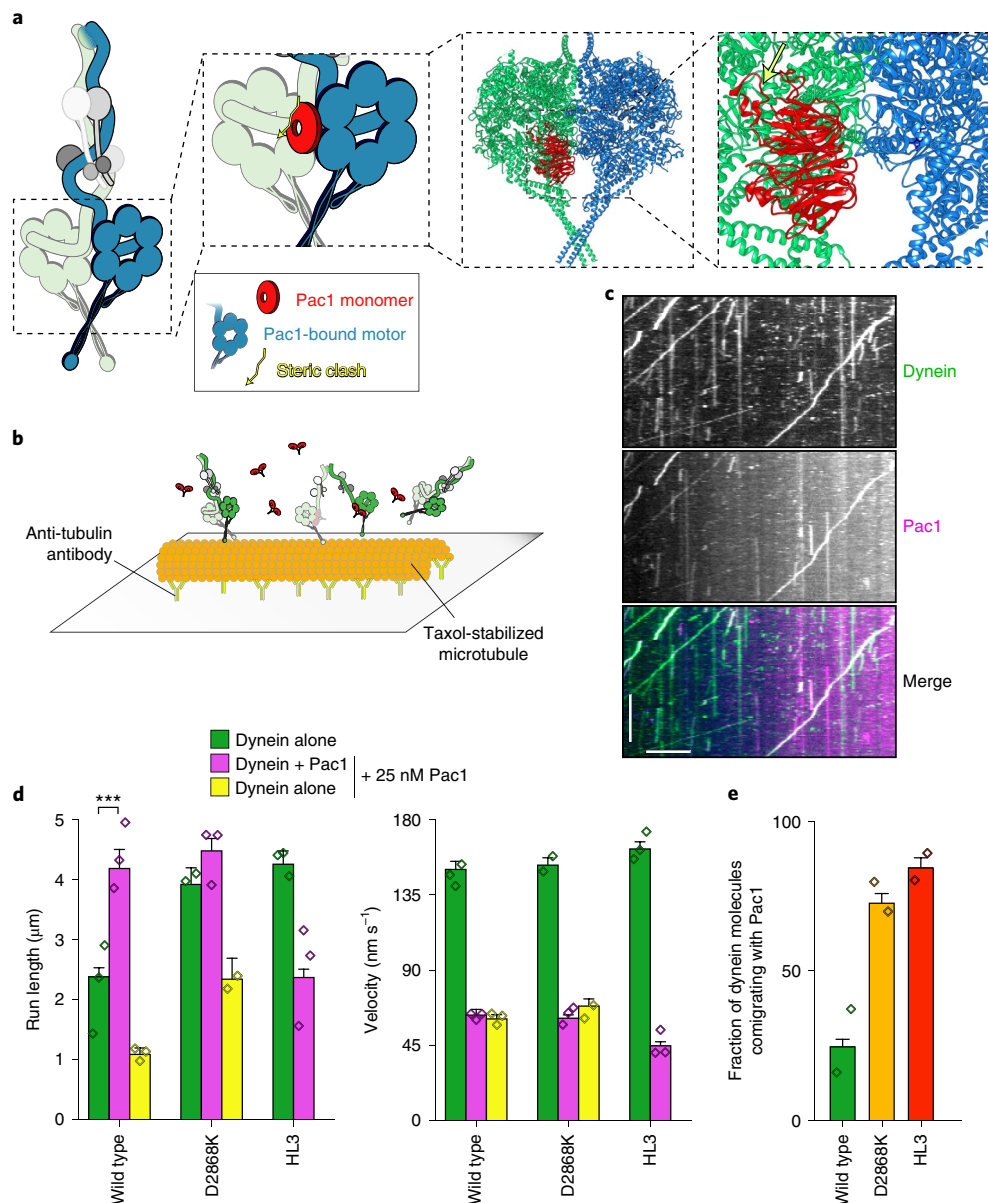


**Fig. 5 | Pac1 promotes the release of the autoinhibited conformation of dynein.** **a**, Cartoon and structural model showing the steric clash between autoinhibited dynein and Pac1. The structural model was generated by aligning the Pac1-bound dynein monomer structure (PDB 5VH9 (ref. 28)) into one of the heavy chains in the phi-particle structure (PDB 5NVU<sup>4</sup>). Note the steric clash (indicated by jagged yellow arrow) between Pac1 (red) and the non-Pac1-bound heavy chain (green). **b**, The experimental setup for the dynein–Pac1 single-molecule assay. **c**, Representative kymograph showing comigrating dynein–Pac1 complexes in motility buffer supplemented with 150 mM potassium acetate (the *n* values are provided in **d** and **e**). Scale bars, 4  $\mu$ m (horizontal) and 2 min (vertical). **d**, Plots showing motility parameters (including mean run-length values, from fitting of raw data to one-phase decay (left) and velocity (right)) of indicated dyneins moving in the absence (that is, those not pre-incubated with Pac1, green) or presence of 25 nM Pac1 (dimer concentration). The error bars indicate s.e. For those experiments in which Pac1 and dynein were preincubated, we separately scored those dyneins comigrating with Pac1 (magenta) or migrating without Pac1 (yellow); from left to right, wild-type: *n* = 437, *n* = 353 and *n* = 553 dyneins  $\pm$  Pac1 from three independent replicates; D2868K: *n* = 329, *n* = 664 and *n* = 134 dyneins  $\pm$  Pac1 from two, three and two independent replicates, respectively; HL3: *n* = 595 and *n* = 416 dyneins  $\pm$  Pac1 from two independent replicates. The diamonds represent mean values obtained from each independent replicate experiment. To acquire videos of dynein alone, durations of 1 s were used; however, for two-colour dynein + Pac1 videos, we used durations of 3 s owing to the speed limitations of our microscope. Statistical significance was determined using two-tailed Mann–Whitney *U*-tests; \*\*\**P* < 0.0001. **e**, The fraction of dynein molecules comigrating with a bound Pac1 was plotted for the indicated dyneins. The error bars show s.e. of proportion; from left to right, *n* = 665, *n* = 398 and *n* = 376 dynein molecules from two independent experiment. The diamonds represent mean values obtained from each independent replicate experiment (Extended Data Figs. 6 and 7).

indicate that Pac1 indeed stabilizes an uninhibited conformation of motile dynein complexes.

By incubating HALO<sup>488</sup>–dynein with an equimolar mixture of Pac1–SNAP<sup>647</sup> and Pac1–SNAP<sup>561</sup>, we found that the large majority of dynein–Pac1 complexes possessed only one Pac1 dimer, and only

a small number were bound to two (5.7% after correcting for those dynein complexes that are migrating with two Pac1 dimers of the same colour; Extended Data Fig. 7a,b). Thus, although dynein can bind to two Pac1 dimers, this is a low probability event. We noted no significant difference in either run length or velocity values for



dyneins bound to 1 Pac1 dimer versus 2 Pac1 dimers (Extended Data Fig. 7b).

**Pac1-mediated reduction in dynein velocity requires non-specific Pac1–microtubule interaction.** We next sought to clarify the prevailing model for Pac1 in dynein velocity reduction<sup>26,27,29</sup>. We hypothesized that Pac1 reduces dynein velocity as a direct consequence of its ability to bind to both dynein and microtubules (as with the microtubule-associated protein She1 (ref. 48)). Consistent with this possibility, structural analysis revealed that Pac1 binds to dynein at a region that is proximal to the microtubule (Extended Data Fig. 7c,d). Our first evidence that this may be the case was obtained by separately analysing dynein complexes that comigrated with Pac1 versus those that did not (Fig. 5d, yellow versus magenta bars). Dynein complexes that comigrated with Pac1 moved with the same reduction in velocity as those that did not (Fig. 5d). Moreover, those dyneins that moved with two bound Pac1 dimers did not move at a lower velocity than those dyneins bound to one Pac1 dimer (Extended Data Fig. 7b), suggesting that Pac1 binding does not directly affect dynein mechanochemistry. These data indicate that although processivity enhancement of dynein by Pac1 occurs in a manner that requires a stable dynein–Pac1 complex, velocity reduction does not.

Given the low but detectable Pac1–microtubule binding in these conditions (Extended Data Fig. 6a,b) we sought to further minimize Pac1–microtubule binding. Supplementing the buffer with 150 mM potassium chloride reduced Pac1–microtubule binding to almost background levels (Extended Data Fig. 6a,b,h), yet did not negatively impact the Pac1–dynein interaction, as assessed from two-colour imaging of dynein<sup>D2868K</sup> and Pac1 (Fig. 6a; an identical ionic strength buffer was also used previously to assess dynein–Pac1 interaction<sup>26,27</sup>). By performing the motility assay in varying buffer conditions, we found that the degree to which Pac1 reduces dynein velocity directly correlates with the extent of Pac1–microtubule binding (Fig. 6b–d, Extended Data Fig. 7e,g), which we further confirmed by plotting and fitting the relationship to a linear regression (Fig. 6e, blue points;  $R^2=0.8873$ ). Finally, inclusion of cell extracts in the motility chamber—which reduces Pac1–microtubule binding, even in low ionic strength buffers (Extended Data Fig. 6d,e)—also severely attenuated the velocity-reduction effect (Fig. 6e, yellow point; Extended Data Fig. 6f,g). Thus, in contrast to processivity enhancement by Pac1, which occurs in a manner that is independent of Pac1–microtubule binding, velocity reduction of dynein by Pac1 occurs only when Pac1 is bound to microtubules. Taken together, these findings support a model in which Pac1 is not an inhibitor but, rather, an activator of dynein.

## Discussion

We propose the following model for dynein function (Fig. 6f): (1) dynein stochastically switches between autoinhibited and uninhibited states; (2) one or two Pac1 dimers bind to dynein when it is in the uninhibited state, consequently preventing it from switching to the autoinhibited conformation; (3) Pac1–dynein associate with plus ends<sup>49</sup> through Bik1/CLIP-170 (ref. 50; in a manner that does not require the dynein MTBD<sup>43</sup>, as shown); (4) uninhibited plus end-bound dynein interacts with dynactin, where they remain inactive, possibly due to the lack of an adapter at this site<sup>23,25,43</sup>; (5) after encountering cortical Num1, the dynein–dynactin complex is offloaded<sup>29</sup> and activated for motility<sup>43</sup>, possibly due to the arrangement of the motor heads in a parallel manner that is conducive for motility<sup>4</sup>. Note that dynein<sup>HL3</sup> is inactive in cells, despite exhibiting in vitro and localization phenotypes that are similar to other uninhibited mutants<sup>29</sup>. This could be a consequence of the helical linker disrupting the adoption of the parallel head configuration that may be needed for in vivo activity<sup>4</sup>.

Our study indicates that Pac1 promotes dynein activity by stabilizing the uninhibited state, and that previous observations of a velocity-reduction phenotype<sup>26–29</sup> are likely due to the low ionic strength buffers that were used in these assays. Although we observed a small effect of Pac1 on dynein velocity even at higher ionic strengths, this was likely due to residual Pac1–microtubule binding (Extended Data Fig. 6h). These data challenge the current model for Pac1 activity, whereby its binding to the motor domain sterically blocks the mechanochemical cycle of dynein<sup>27</sup>, thereby promoting its association with microtubule plus ends<sup>26–28</sup> (the latter of which is also contradicted by the dispensable nature of the dynein MTBD for plus end localization<sup>43</sup>). Our data indicate that Pac1 reduces dynein velocity in low ionic strength buffers by exerting drag on dynein through simultaneous contacts with dynein and microtubules, similar to observations with the microtubule-associated protein She1 (ref. 48). This raises the question of whether microtubule binding by Pac1 is a relevant activity in cells. Several lines of evidence indicate that this is not the case. Pac1 localizes only to plus ends in cells, and not along microtubules<sup>44,49,51</sup>. The plus end binding of Pac1 is indirect, as it is dependent on dynein<sup>49</sup> and Bik1/CLIP-170 (refs. 49,51). Finally, studies have observed no microtubule-binding activity of LIS1 (refs. 21,23–25). In fact, in contrast to an inhibitory function, two of these studies observed a LIS1-dependent increase in dynein–dynactin velocity<sup>23,24</sup> for reasons that have now been determined by two new studies in this issue<sup>52,53</sup>: by stabilizing uninhibited dynein, LIS1 promotes the assembly of

**Fig. 6 | Reducing Pac1–microtubule binding minimizes the Pac1-mediated reduction of dynein velocity.** **a**, Representative kymographs depicting comigrating dynein<sup>D2868K</sup>–Pac1 complexes in motility buffers with increased ionic strength, from three (top) and two (bottom) independent replicates. Note that Pac1 and dynein still interact robustly in these conditions, as apparent from the high degree of persistent colocalization. **b,c**, Representative kymographs showing different motility characteristics of GST–dynein<sup>MOTOR</sup> (used extensively in previous Pac1 studies<sup>26–28</sup>) in the presence of Pac1 when Pac1 is either extensively bound to the microtubule (**b**) or to a much less extent (**c**); the *n* values are provided in **d**. For **a–c**, scale bars, 4  $\mu$ m (horizontal) and 2 min (vertical). **d**, Mean normalized motility parameters (means from independent replicates as well as scatter plots are provided in Extended Data Fig. 7e–g) of GST–dynein<sup>MOTOR</sup> in the absence (green) or presence (magenta) of 25 nM Pac1 (dimer concentration); from left to right, *n* = 348, *n* = 268, *n* = 396, *n* = 226, *n* = 447, *n* = 359, *n* = 385, *n* = 315, *n* = 251 and *n* = 320 motors from two independent experiments each. The error bars indicate s.e. **e**, Relative degree of Pac1–microtubule binding (mean values normalized to 1; the scatter plot of intensity values as well as the *n* values for each are provided in Extended Data Fig. 6b,e) versus mean relative velocity of GST–dynein<sup>MOTOR</sup> in the presence of Pac1 (mean GST–dynein<sup>MOTOR</sup> velocity in the absence of Pac1 equals 1; the relative and absolute velocity values as well as *n* values are provided in **d** and Extended Data Figs. 6f,g and 7e–g). The blue and yellow points are from the increasing ionic strength buffer experiment (shown in **d**), and the cell extract experiment (Extended Data Fig. 6d–g), respectively. The error bars represent s.e. The blue points were fit to a linear regression, and the  $R^2$  value is shown. **f**, Model for dynein and Pac1 activity in cells: dynein stochastically switches between closed and open states (i), the latter of which is stabilized by Pac1 binding (ii); dynein–Pac1 associates with plus ends through direct interactions with Bik1 (iii), which may rely in part on Bim1. Plus end dynein–Pac1 associates with dynactin (iv), which is then offloaded to cortical Num1 (v). Given the lack of apparent Pac1 cortical foci, Pac1 likely dissociates either concomitant with, or subsequent to dynein–dynactin offloading (Extended Data Fig. 7).

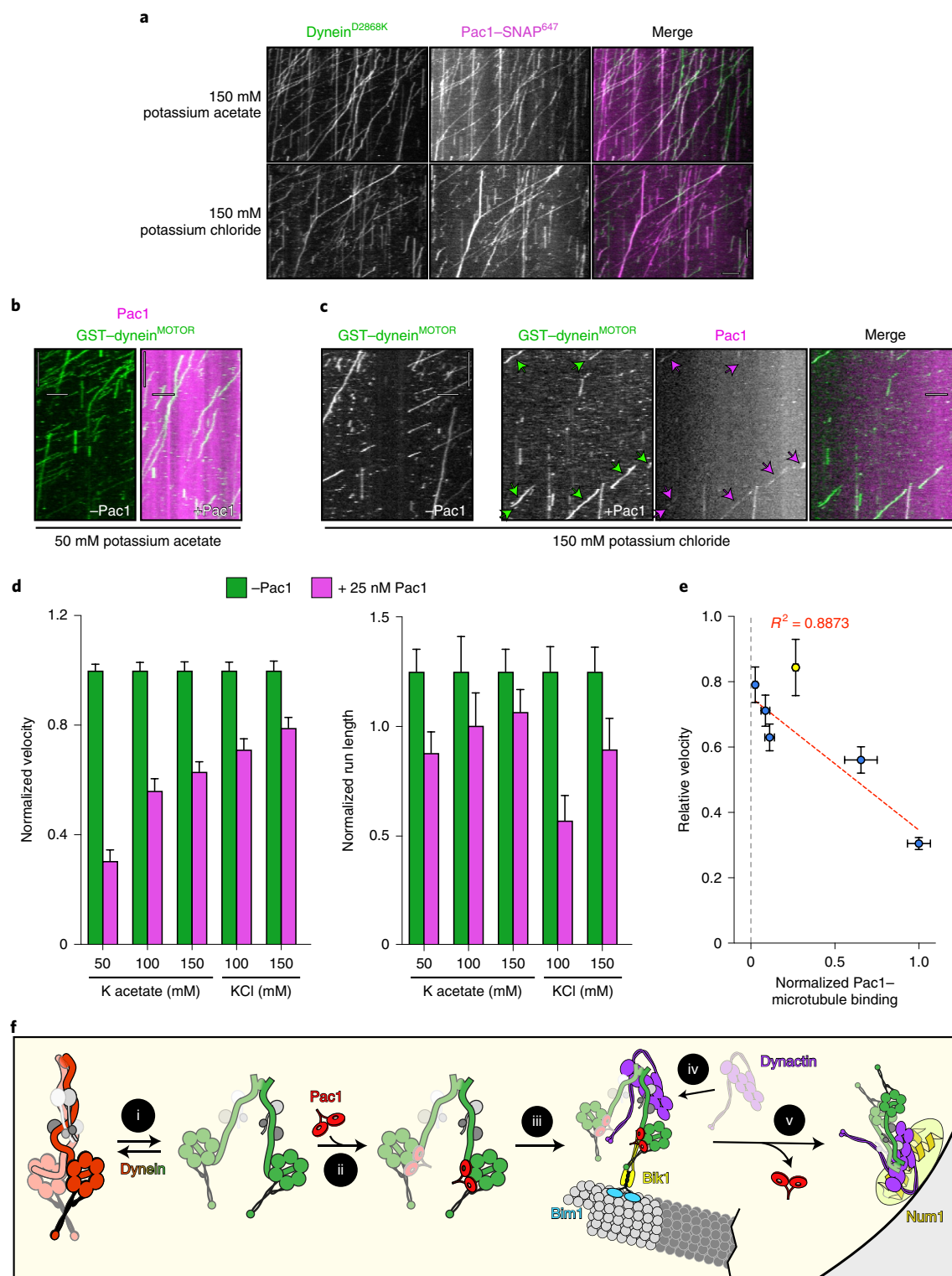
faster 2 dynein:1 dynactin complexes<sup>54</sup>. Several studies demonstrate the conserved nature of the autoinhibitory mechanism<sup>6,7</sup>, including a recent study in *Aspergillus nidulans*<sup>55</sup>.

Our findings raise interesting questions regarding the distinct motility capabilities of yeast versus human dynein, the latter of which requires dynactin and an adapter for processive motility<sup>1,2</sup>. In particular, why does yeast dynein not need such factors despite its high propensity to adopt the autoinhibited state? Perhaps the yeast dynein motor domains are more likely to orient in a parallel configuration<sup>4</sup> in the absence of dynactin binding?

Higher-resolution structural data will be required to determine whether this is indeed the case.

### Online content

Any methods, additional references, Nature Research reporting summaries, source data, extended data, supplementary information, acknowledgements, peer review information; details of author contributions and competing interests; and statements of data and code availability are available at <https://doi.org/10.1038/s41556-020-0492-1>.



Received: 15 May 2019; Accepted: 23 February 2020;  
Published online: 27 April 2020

## References

- Schlager, M. A., Hoang, H. T., Urnavicius, L., Bullock, S. L. & Carter, A. P. In vitro reconstitution of a highly processive recombinant human dynein complex. *EMBO J.* **33**, 1855–1868 (2014).
- McKenney, R. J., Huynh, W., Tanenbaum, M. E., Bhabha, G. & Vale, R. D. Activation of cytoplasmic dynein motility by dynactin-cargo adapter complexes. *Science* **345**, 337–341 (2014).
- McKenney, R. J., Huynh, W., Vale, R. D. & Sirajuddin, M. Tyrosination of  $\alpha$ -tubulin controls the initiation of processive dynein-dynactin motility. *EMBO J.* **35**, 1175–1185 (2016).
- Zhang, K. et al. Cryo-EM reveals how human cytoplasmic dynein is auto-inhibited and activated. *Cell* **169**, 1303–1314 (2017).
- Amos, L. A. Brain dynein crossbridges microtubules into bundles. *J. Cell Sci.* **93**, 19–28 (1989).
- Toropova, K., Mladenov, M. & Roberts, A. J. Intraflagellar transport dynein is autoinhibited by trapping of its mechanical and track-binding elements. *Nat. Struct. Mol. Biol.* **24**, 461–468 (2017).
- Jordan, M. A., Diener, D. R., Stepanek, L. & Pigino, G. The cryo-EM structure of intraflagellar transport trains reveals how dynein is inactivated to ensure unidirectional anterograde movement in cilia. *Nat. Cell Biol.* **20**, 1250–1255 (2018).
- Torisawa, T. et al. Autoinhibition and cooperative activation mechanisms of cytoplasmic dynein. *Nat. Cell Biol.* **16**, 1118–1124 (2014).
- Reck-Peterson, S. L. et al. Single-molecule analysis of dynein processivity and stepping behavior. *Cell* **126**, 335–348 (2006).
- Kardon, J. R., Reck-Peterson, S. L. & Vale, R. D. Regulation of the processivity and intracellular localization of *Saccharomyces cerevisiae* dynein by dynactin. *Proc. Natl Acad. Sci. USA* **106**, 5669–5674 (2009).
- Sasaki, S. et al. A LIS1/NUDEL/cytoplasmic dynein heavy chain complex in the developing and adult nervous system. *Neuron* **28**, 681–696 (2000).
- Wynshaw-Boris, A. & Gambello, M. J. LIS1 and dynein motor function in neuronal migration and development. *Genes Dev.* **15**, 639–651 (2001).
- Moughamian, A. J., Osborn, G. E., Lazarus, J. E., Maday, S. & Holzbaur, E. L. Ordered recruitment of dynactin to the microtubule plus-end is required for efficient initiation of retrograde axonal transport. *J. Neurosci.* **33**, 13190–13203 (2013).
- Raaijmakers, J. A., Tanenbaum, M. E. & Medema, R. H. Systematic dissection of dynein regulators in mitosis. *J. Cell Biol.* **201**, 201–215 (2013).
- Coquelle, F. M. et al. LIS1, CLIP-170's key to the dynein/dynactin pathway. *Mol. Cell. Biol.* **22**, 3089–3102 (2002).
- Tsai, J. W., Bremner, K. H. & Vallee, R. B. Dual subcellular roles for LIS1 and dynein in radial neuronal migration in live brain tissue. *Nat. Neurosci.* **10**, 970–979 (2007).
- Tsai, J. W., Chen, Y., Kriegstein, A. R. & Vallee, R. B. LIS1 RNA interference blocks neural stem cell division, morphogenesis, and motility at multiple stages. *J. Cell Biol.* **170**, 935–945 (2005).
- Yi, J. Y. et al. High-resolution imaging reveals indirect coordination of opposite motors and a role for LIS1 in high-load axonal transport. *J. Cell Biol.* **195**, 193–201 (2011).
- Chapman, D. E. et al. Regulation of in vivo dynein force production by CDK5 and 14-3-3 $\epsilon$  and KIAA0528. *Nat. Commun.* **10**, 228 (2019).
- Reddy, B. J. et al. Load-induced enhancement of dynein force production by LIS1-NudE in vivo and in vitro. *Nat. Commun.* **7**, 12259 (2016).
- McKenney, R. J., Vershinin, M., Kunwar, A., Vallee, R. B. & Gross, S. P. LIS1 and NudE induce a persistent dynein force-producing state. *Cell* **141**, 304–314 (2010).
- Yamada, M. et al. LIS1 and NDEL1 coordinate the plus-end-directed transport of cytoplasmic dynein. *EMBO J.* **27**, 2471–2483 (2008).
- Baumbach, J. et al. Lissencephaly-1 is a context-dependent regulator of the human dynein complex. *eLife* **6**, e21768 (2017).
- Gutierrez, P. A., Ackermann, B. E., Vershinin, M. & McKenney, R. J. Differential effects of the dynein-regulatory factor Lissencephaly-1 on processive dynein-dynactin motility. *J. Biol. Chem.* **292**, 12245–12255 (2017).
- Jha, R., Roostalu, J., Cade, N. I., Trokter, M. & Surrey, T. Combinatorial regulation of the balance between dynein microtubule end accumulation and initiation of directed motility. *EMBO J.* **36**, 3387–3404 (2017).
- Huang, J., Roberts, A. J., Leschziner, A. E. & Reck-Peterson, S. L. Lis1 acts as a “clutch” between the ATPase and microtubule-binding domains of the dynein motor. *Cell* **150**, 975–986 (2012).
- Toropova, K. et al. Lis1 regulates dynein by sterically blocking its mechanochemical cycle. *eLife* **3**, e03372 (2014).
- DeSantis, M. E. et al. Lis1 has two opposing modes of regulating cytoplasmic dynein. *Cell* **170**, 1197–1208 (2017).
- Markus, S. M. & Lee, W. L. Regulated offloading of cytoplasmic dynein from microtubule plus ends to the cortex. *Dev. Cell* **20**, 639–651 (2011).
- Dix, C. I. et al. Lissencephaly-1 promotes the recruitment of dynein and dynactin to transported mRNAs. *J. Cell Biol.* **202**, 479–494 (2013).
- Wang, S. et al. Nudel/NudE and Lis1 promote dynein and dynactin interaction in the context of spindle morphogenesis. *Mol. Biol. Cell* **24**, 3522–3533 (2013).
- Marzo, M. G. et al. Molecular basis for dyneinopathies reveals insight into dynein regulation and dysfunction. *eLife* **8**, e47246 (2019).
- Markus, S. M. & Lee, W. L. Microtubule-dependent path to the cell cortex for cytoplasmic dynein in mitotic spindle orientation. *Bioarchitecture* **1**, 209–215 (2011).
- Schmidt, H., Gleave, E. S. & Carter, A. P. Insights into dynein motor domain function from a 3.3 Å crystal structure. *Nat. Struct. Mol. Biol.* **19**, 492–497 (2012).
- Carter, A. P., Cho, C., Jin, L. & Vale, R. D. Crystal structure of the dynein motor domain. *Science* **331**, 1159–1165 (2011).
- Schmidt, H., Zalyte, R., Urnavicius, L. & Carter, A. P. Structure of human cytoplasmic dynein-2 primed for its power stroke. *Nature* **518**, 435–438 (2015).
- Gibbons, I. R. et al. The affinity of the dynein microtubule-binding domain is modulated by the conformation of its coiled-coil stalk. *J. Biol. Chem.* **280**, 23960–23965 (2005).
- Kon, T. et al. Helix sliding in the stalk coiled coil of dynein couples ATPase and microtubule binding. *Nat. Struct. Mol. Biol.* **16**, 325–333 (2009).
- Rao, L., Berger, F., Nicholas, M. P. & Gennerich, A. Molecular mechanism of cytoplasmic dynein tension sensing. *Nat. Commun.* **10**, 3332 (2019).
- Gennerich, A., Carter, A. P., Reck-Peterson, S. L. & Vale, R. D. Force-induced bidirectional stepping of cytoplasmic dynein. *Cell* **131**, 952–965 (2007).
- Moore, J. K., Li, J. & Cooper, J. A. Dynactin function in mitotic spindle positioning. *Traffic* **9**, 510–527 (2008).
- Markus, S. M., Punch, J. J. & Lee, W. L. Motor- and tail-dependent targeting of dynein to microtubule plus ends and the cell cortex. *Curr. Biol.* **19**, 196–205 (2009).
- Lammers, L. G. & Markus, S. M. The dynein cortical anchor Num1 activates dynein motility by relieving Pac1/LIS1-mediated inhibition. *J. Cell Biol.* **211**, 309–322 (2015).
- Lee, W. L., Oberle, J. R. & Cooper, J. A. The role of the lissencephaly protein Pac1 during nuclear migration in budding yeast. *J. Cell Biol.* **160**, 355–364 (2003).
- Yin, H., Pruyne, D., Huffer, T. C. & Bretscher, A. Myosin V orientates the mitotic spindle in yeast. *Nature* **406**, 1013–1015 (2000).
- Hwang, E., Kusch, J., Barral, Y. & Huffer, T. C. Spindle orientation in *Saccharomyces cerevisiae* depends on the transport of microtubule ends along polarized actin cables. *J. Cell Biol.* **161**, 483–488 (2003).
- Liakopoulos, D., Kusch, J., Grava, S., Vogel, J. & Barral, Y. Asymmetric loading of Kar9 onto spindle poles and microtubules ensures proper spindle alignment. *Cell* **112**, 561–574 (2003).
- Ecklund, K. H. et al. She1 affects dynein through direct interactions with the microtubule and the dynein microtubule-binding domain. *Nat. Commun.* **8**, 2151 (2017).
- Markus, S. M. et al. Quantitative analysis of Pac1/LIS1-mediated dynein targeting: implications for regulation of dynein activity in budding yeast. *Cytoskeleton* **68**, 157–174 (2011).
- Sheeman, B. et al. Determinants of *S. cerevisiae* dynein localization and activation: implications for the mechanism of spindle positioning. *Curr. Biol.* **13**, 364–372 (2003).
- Li, J., Lee, W. L. & Cooper, J. A. Nudel targets dynein to microtubule ends through LIS1. *Nat. Cell Biol.* **7**, 686–690 (2005).
- Elshenawy, M. M. et al. Lis1 activates dynein motility by pairing it with dynactin. *Nat. Cell Biol.* <https://doi.org/10.1038/s41556-020-0501-4> (2020).
- Htet, Z. M. et al. Lis1 promotes the formation of activated cytoplasmic dynein-1 complexes. *Nat. Cell Biol.* <https://doi.org/10.1038/s41556-020-0506-z> (2020).
- Urnavicius, L. et al. Cryo-EM shows how dynactin recruits two dyneins for faster movement. *Nature* **554**, 202–206 (2018).
- Qiu, R., Zhang, J. & Xiang, X. LIS1 regulates cargo-adapter-mediated activation of dynein by overcoming its autoinhibition in vivo. *J. Cell Biol.* **218**, 3630–3646 (2019).
- Curran, K. A. et al. Short synthetic terminators for improved heterologous gene expression in yeast. *ACS Synth. Biol.* **4**, 824–832 (2015).
- Kelley, L. A., Mezulis, S., Yates, C. M., Wass, M. N. & Sternberg, M. J. The Phyre2 web portal for protein modeling, prediction and analysis. *Nat. Protoc.* **10**, 845–858 (2015).
- Poirier, K. et al. Mutations in *TUBG1*, *DYNC1H1*, *KIF5C* and *KIF2A* cause malformations of cortical development and microcephaly. *Nat. Genet.* **45**, 639–647 (2013).
- Scoto, M. et al. Novel mutations expand the clinical spectrum of *DYNC1H1*-associated spinal muscular atrophy. *Neurology* **84**, 668–679 (2015).
- Willemsen, M. H. et al. Mutations in *DYNC1H1* cause severe intellectual disability with neuronal migration defects. *J. Med. Genet.* **49**, 179–183 (2012).
- Heil-Chapdelaine, R. A., Oberle, J. R. & Cooper, J. A. The cortical protein Num1p is essential for dynein-dependent interactions of microtubules with the cortex. *J. Cell Biol.* **151**, 1337–1344 (2000).

**Publisher's note** Springer Nature remains neutral with regard to jurisdictional claims in published maps and institutional affiliations.

© The Author(s), under exclusive licence to Springer Nature Limited 2020



## Methods

**Media and strain construction.** The strains used here (listed in Supplementary Table 1) were derived from either W303 or YEF473 and are available upon request. We transformed yeast strains using the lithium acetate method. Strains carrying mutations were constructed using PCR product-mediated transformation, or by mating followed by tetrad dissection. Proper tagging and mutagenesis was confirmed using PCR analysis and, in most cases, sequencing (all of the point mutations were confirmed by sequencing). Fluorescent tubulin-expressing yeast strains were generated using common strategies. Strains overexpressing the yeast dynein complex (or the GST-dynein<sup>MOTOR</sup> fragment) were generated by transforming p8His-ZZ-SNAPf-Dynein, p8His-ZZ-HALO-Dynein or pZZ-dynein<sup>MOTOR</sup>-HALO (wild-type or mutants; see below) linearized by digestion with *ApaI* (cuts within *URA3*; Fig. 1a). Integration was confirmed using PCR analysis. Yeast synthetic defined (SD) medium was obtained from Sunrise Science Products.

**Plasmid generation.** To overexpress and purify the yeast dynein complex (wild type or mutants), we generated a polycistronic plasmid expressing all four subunits of the dynein complex using strategies analogous to the biGBAC assembly<sup>62</sup>. We first generated a yeast expression library vector, pLIBy, which enables the generation of gene expression cassettes (GEC) with a strong inducible *GAL1* promoter (*GAL1p*) at the 5' end and a synthetic terminator sequence (*T<sub>synth3</sub>* (ref. 56)) at the 3' end. A PCR product encompassing *GAL1p*, and an oligonucleotide containing *T<sub>synth3</sub>* and a multicloning site (*XbaI*-*NotI*-*SpeI*-*BamHI*) were assembled into pRS305 digested with *BamHI* and *NotI* using Gibson assembly, yielding pLIBy. We also generated a yeast genomic-integration vector with optimized linker sequences for Gibson assembly<sup>62</sup> flanked by *PmeI* restriction sites (equivalent to pbiG1a and pbiG1b). These plasmids—pbiG1ay and pbiG1by—were generated using Gibson assembly to insert a PCR product encompassing these elements from pbiG1a and pbiG1b<sup>62</sup> into pRS306. PCR products encompassing the *DYN2* (without the native intron), *DYN3* or *PAC11* open reading frames were assembled into pLIBy digested with *BamHI* and *NotI*. Subsequently, these GECs were amplified from each respective pLIBy vector using oligonucleotides that include regions for priming preceded on the 5' end by predefined 'Cas' sequences<sup>62</sup>; the *DYN2* GEC was amplified using *Casα*-forward and *Casβ*-reverse; the *DYN3* GEC was amplified using *Casβ*-forward and *Casγ*-reverse; and the *PAC11* GEC was amplified using *Casγ*-forward and *Casα*-reverse. These three PCR products were assembled into pbiG1by digested with *SwaI* to generate pbiG1by:*GAL1p*:*Dyn2::GAL1p*:*DYN3::GAL1p*:*PAC11*.

We generated pLIBy:6His-*StreptII*-SNAPf-*DYN1* using Gibson assembly. However, owing to complications with generating a PCR product from this vector, we chose to clone everything into this vector. We first substituted the *LEU2* expression cassette in the pLIBy backbone with a *URA3* marker by assembling a PCR product encompassing the *URA3* cassette from pRS306 into pLIBy:6His-*StreptII*-SNAPf-*DYN1* digested with *KasI* and *AatII*, yielding pLIBy:6His-*StreptII*-SNAPf-*DYN1::URA3*. To enable assembly of the *DYN2/DYN3/PAC11* polygene cassette into pLIBy:6His-*StreptII*-SNAPf-*DYN1::URA3*, we inserted the optimized B and C linker sequences for Gibson assembly<sup>62</sup> into this plasmid by assembling a PCR product encompassing B-*PmeI* site-C into pLIBy:6His-*StreptII*-SNAPf-*DYN1::URA3* digested with *KpnI* and *Sall*. After digesting with *PmeI*, this plasmid was assembled with the *PmeI* restriction digest product from pbiG1by:*GAL1p*:*Dyn2::GAL1p*:*DYN3::GAL1p*:*PAC11* (encompassing *GAL1p*:*Dyn2::GAL1p*:*DYN3::GAL1p*:*PAC11*), yielding pLIBy: *GAL1p*:*Dyn2::GAL1p*:*DYN3::GAL1p*:*PAC11::GAL1p*:6His-*StreptII*-SNAPf-*Dyn1::URA3*; hereafter referred to as p6His-*StreptII*-SNAPf-Dynein. Before using this plasmid for pilot tests, we decided to swap the 6His-*StreptII* affinity tag for an 8His-ZZ tag (followed by a tandem TEV protease recognition site). We did this by assembling a PCR product encompassing 8His-ZZ into p6His-*StreptII*-SNAPf-Dynein digested with *AatII* and *XhoI*, yielding p8His-ZZ-SNAPf-Dynein. We replaced the SNAPf tag with a HALO tag using a similar strategy, yielding p8His-ZZ-HALO-Dynein. All of the mutations were engineered into these plasmids using common strategies.

Owing to difficulties in engineering the D2868K mutation into the GST-dynein<sup>MOTOR</sup>-expressing yeast strain (SMY1008), we generated a plasmid that overexpresses this fragment in yeast (under the control of the *GAL1* promoter; Extended Data Fig. 3a). Similar to the full-length dynein complex expression plasmids described above, this plasmid can also be integrated into the *ura3-1* locus. PCR products encompassing the entire *GAL1p*:ZZ-TEV-6His-GFP-GST-dyn1<sup>MOTOR</sup>-HALO cassette (comprised of 4 individual pieces, each with 23 nucleotides of overlapping sequences; amplified from SMY1008) were assembled into pRS305 digested with *KpnI* and *BamHI* using Gibson assembly, yielding pZZ-dynein<sup>MOTOR</sup>-HALO. The D2868K mutation was engineered into this plasmid using common strategies.

**Protein purification.** Purification of yeast dynein (ZZ-TEV-Dyn1-HALO, under the native *DYN1* promoter; ZZ-TEV-HALO-(or SNAPf)-Dynein, with all genes under the control of the *GAL1p* promoter; or ZZ-TEV-6His-GFP-3HA-GST-dynein<sup>MOTOR</sup>-HALO, under the control of the *GAL1p* promoter) was performed as previously described with minor modifications used for the overexpressed complex<sup>48</sup>. In brief, yeast cultures were grown in YPA medium supplemented with either 2% glucose (for non-overexpressed full-length dynein) or 2% galactose (for

the *GAL1p*-inducible strains; overexpression of the full-length dynein complex was induced for no more than 3 h), collected, washed with cold water and then resuspended in a small volume of water. The resuspended cell pellet was drop-frozen into liquid nitrogen and then lysed in a coffee grinder (Hamilton Beach). For most purifications (with the exception of those used for negative stain EM imaging) we used the following procedure: after lysis, 0.25 volumes of 4× dynein lysis buffer (1× buffer: 30 mM HEPES pH 7.2, 50 mM potassium acetate, 2 mM magnesium acetate, 0.2 mM EGTA) supplemented with 1 mM dithiothreitol (DTT), 0.1 mM Mg-ATP and 0.5 mM Pefabloc SC (concentrations for the 1× buffer), and the lysate was clarified by centrifugation at 22,000g for 20 min. The supernatant was then bound to IgG sepharose 6 fast flow resin (GE) for 1–1.5 h at 4°C, which was subsequently washed three times in 5 ml lysis buffer, and twice in 5 ml TEV buffer (50 mM Tris pH 8.0, 150 mM potassium acetate, 2 mM magnesium acetate, 1 mM EGTA and 10% glycerol) supplemented with 0.005% Triton X-100, 1 mM DTT, 0.1 mM Mg-ATP and 0.5 mM Pefabloc SC. To fluorescently label the motors for single-molecule analyses, the bead-bound protein was incubated with either 6.7 μM HaloTag-AlexaFluor660, HaloTag-AlexaFluor488, HaloTag-TMR (Promega), or SNAP-Surface Alex Fluor 647 (NEB), as appropriate, for 10–20 min at room temperature. The resin was then washed four more times in TEV buffer supplemented with 1 mM DTT, 0.005% Triton X-100 and 0.1 mM Mg-ATP, and then incubated with TEV protease for 1–1.5 h at 16°C. After digestion with TEV, the beads were pelleted, and the resulting supernatant was collected, aliquoted, flash-frozen in liquid nitrogen, and stored at –80°C. Protein preparations used for negative stain EM imaging were tandem-affinity purified. To do so, subsequent to lysis, 0.25 volumes of 4× NiNTA dynein lysis buffer (1× buffer: 30 mM HEPES pH 7.2, 200 mM potassium acetate, 2 mM magnesium acetate and 10% glycerol) supplemented with 1 mM beta-mercaptoethanol, 0.1 mM Mg-ATP and 0.5 mM Pefabloc SC (concentrations for the 1× buffer) was added, and the lysate was clarified as described above. The supernatant was then bound to NiNTA agarose for 1 h at 4°C, which was subsequently washed three times in 5 ml NiNTA lysis buffer. The protein was eluted in NiNTA lysis buffer supplemented with 250 mM imidazole by incubation for 10 min on ice. The eluate was then diluted with an equal volume of dynein lysis buffer, which was then incubated with IgG sepharose 6 fast flow resin for 1 h at 4°C. The beads were washed and the protein was eluted as described above (with TEV protease). Eluted protein was either applied to a size-exclusion resin (Superose 6; GE) or snap-frozen. The gel filtration resin was equilibrated in GF150 buffer (25 mM HEPES pH 7.4, 150 mM KCl, 1 mM MgCl<sub>2</sub>, 5 mM DTT and 0.1 mM Mg-ATP) using an AKTA Pure system. Peak fractions (determined by absorbance at 260 nm and SDS-PAGE) were pooled, concentrated, aliquoted, flash-frozen and then stored at –80°C. We noted that prolonged periods of storage at –80°C (≥3–5 d) led to an increase in the prevalence of dynein aggregates (as apparent from fluorescence intensity analysis), which exhibited longer run lengths in single-molecule assays. We also noted that aggregation was more pronounced when the motor was labelled with HaloTag-AlexaFluor660 than it was with HaloTag-AlexaFluor488.

Purification of Pac1-Flag-SNAP was performed as previously described<sup>26</sup>, with the addition of a gel filtration step to remove any residual, unbound fluorescent dye. Specifically, TEV protease-eluted protein was applied to a size exclusion resin (Superose 6; GE) that was equilibrated in TEV buffer supplemented with 1 mM DTT using an AKTA Pure. Peak fractions (determined by absorbance at 260 nm and SDS-PAGE) were pooled, concentrated, aliquoted, flash-frozen and then stored at –80°C.

For comparison of elution profiles between yeast and human dynein complexes, the human dynein complex was expressed and purified from insect cells (ExpiSf9 cells; Life Technologies) as previously described with minor modifications<sup>41</sup>. In brief, 4 ml of ExpiSf9 cells at  $2.5 \times 10^6$  cells per ml, which were maintained in ExpiSf CD Medium (Life Technologies), were transfected with 1 μg of bacmid DNA<sup>32</sup> using ExpiFectamine (Life Technologies) according to the manufacturer's instructions. Then, 5 d after transfection, the cells were pelleted, and 1 ml of the resulting supernatant (P1) was used to infect 300 ml of ExpiSf9 cells ( $5 \times 10^6$  cells per ml). Then, 72 h later, the cells were collected (centrifugation at 2,000g for 20 min), washed with PBS (pH 7.2), pelleted again by centrifugation (1,810g for 20 min) and resuspended in an equal volume of human dynein lysis buffer (50 mM HEPES pH 7.4, 100 mM NaCl, 10% glycerol, 1 mM DTT, 0.1 mM Mg-ATP and 1 mM phenylmethylsulfonyl fluoride). The resulting cell suspension was drop-frozen in liquid nitrogen and stored at –80°C. For protein purification, 30 ml of additional human dynein lysis buffer supplemented with cComplete protease inhibitor cocktail (Roche) was added to the frozen cell pellet, which was then rapidly thawed in a 37°C water bath before incubation on ice. Cells were lysed using a dounce-type tissue grinder (Wheaton) using ≥150 strokes (lysis was monitored by microscopy). Subsequent to clarification using centrifugation at 22,000g for 45 min, the supernatant was applied to 2 ml of IgG sepharose fast flow resin pre-equilibrated in human dynein lysis buffer, and incubated at 4°C for 2–4 h. The beads were then washed with 50 ml of human dynein lysis buffer, and 50 ml of human dynein TEV buffer (50 mM Tris pH 7.4, 150 mM potassium acetate, 2 mM magnesium acetate, 1 mM EGTA, 10% glycerol, 1 mM DTT and 0.1 mM Mg-ATP). The bead-bound protein was eluted by incubation with TEV protease overnight at 4°C. The next morning, the recovered supernatant was applied to a Superose 6 gel filtration column as described above for yeast dynein.



**Single-molecule motility assays.** The yeast dynein single-molecule motility assay was performed as previously described with minor modifications<sup>48</sup>. In brief, flow chambers constructed using slides and plasma cleaned and silanized coverslips attached with double-sided adhesive tape were coated with anti-tubulin antibodies (8 µg ml<sup>-1</sup>, YL1/2; Accurate Chemical & Scientific Corporation) and then blocked with 1% Pluronic F-127 (Fisher Scientific). Taxol-stabilized microtubules assembled from unlabelled and fluorescently labelled porcine tubulin (10:1 ratio; Cytoskeleton) were introduced into the chamber. After incubation for 5–10 min, the chamber was washed with dynein lysis buffer (see above) supplemented with 20 µM taxol. Subsequently, purified dynein motors diluted in motility buffer (30 mM HEPES pH 7.2, 2 mM magnesium acetate, 1 mM EGTA, 1 mM DTT, 1 mM Mg-ATP, 0.05% Pluronic F-127, 20 µM taxol and an oxygen-scavenging system consisting of 1.5% glucose, 1 U ml<sup>-1</sup> glucose oxidase, 125 U ml<sup>-1</sup> catalase) supplemented either with 50 mM potassium acetate or as indicated in figure legends, were introduced into the chamber and imaged.

To image co-migrating Pac1–dynein complexes, 500 nM Pac1–SNAP<sup>647</sup> (dimer concentration) and 10–50 nM HALO<sup>TM</sup>-Dynein were preincubated on ice for 10–15 min before a twenty-fold dilution into modified motility buffer (30 mM HEPES pH 7.2, 2 mM magnesium acetate, 1 mM EGTA, 1 mM DTT and 1 mM Mg-ATP) supplemented with potassium acetate or potassium chloride as indicated in the figure legends, 0.05% Pluronic F-127, 20 µM taxol and an oxygen-scavenging system (as described above). The higher yield overexpressed dynein complex was needed for these assays given the low landing rate of dynein in the higher ionic strength buffers. We ensured that comigrating Pac1–SNAP<sup>647</sup> spots were not due to bleed-through from the HALO<sup>TM</sup>-dynein channel by performing two-colour imaging with HALO<sup>TM</sup>-dynein alone (no spots were apparent in the far-red channel in these cases). To measure Pac1 fluorescence intensity on microtubules, 50 nM of Pac1–SNAP<sup>647</sup> (dimer concentration) diluted in motility buffer was added to chambers containing taxol-stabilized microtubules.

To remove the unstructured E-hooks from microtubules, taxol-stabilized microtubules were digested with a 1 mg ml<sup>-1</sup> subtilisin (Sigma-Aldrich) for 90 min at 37°C before the flow chambers were prepared. For experiments in which cellular extracts were included in the imaging chamber (Extended Data Fig. 6d,e), log-phase cultures of SMY2532 (cells that do not express dynein; Supplementary Table 1) were pelleted, resuspended in a small volume of motility buffer (with 50 mM potassium acetate), drop-frozen in liquid nitrogen, lysed using pestle and mortar, and then clarified using centrifugation at 21,000g for 15 min. To assess Pac1–microtubule binding in the presence of cell extracts, 50 nM Pac1–SNAP<sup>647</sup> (dimer concentration) was diluted in motility buffer supplemented with clarified extract (0.96 mg ml<sup>-1</sup> final concentration) and introduced into an imaging chamber. Similar conditions were used to assess the effect of Pac1 on dynein motility in the presence of cell extract, except 25 nM Pac1 and ~50 pM GST–dynein<sup>MOTOR</sup> were also included in the imaging chamber; moreover, ATP levels were increased to 10 mM (compared with 1 mM, which was used for the other single-molecule assays).

Total internal reflection fluorescence microscopy images were collected using a ×100/1.49 NA TIRF objective on a Nikon Ti-E inverted microscope equipped with a Ti-S-E motorized stage, piezo Z-control (Physik Instrumente) and an iXon X3 DU897 cooled EM-CCD camera (Andor). We used 488 nm, 561 nm and 640 nm lasers (Coherent) along with a multi-pass quad filter cube set (C-TIRF for 405 nm/488 nm/561 nm/638 nm; Chroma) and emission filters were mounted in a filter wheel (525 nm/50 nm, 600 nm/50 nm and 700 nm/75 nm; Chroma). To image non-fluorescent microtubules (Extended Data Fig. 6d), we used interference reflection microscopy, as previously described<sup>49</sup>. For time-lapse videos, we acquired images at intervals of 1 s, 2 s or 3 s for 8–10 min. Velocity and run-length values were determined from kymographs generated using the MultipleKymograph plugin for ImageJ ([http://www.embl.de/eamnet/html/body\\_kymograph.html](http://www.embl.de/eamnet/html/body_kymograph.html)). The motors that moved for at least three time points were measured. Reported run lengths were determined by fitting raw values to a one-phase decay.

**Negative stain EM and image analysis.** EM grids were prepared using a standard negative stain protocol by applying fresh dynein samples to glow-discharged carbon-coated 200 mesh copper grids. After incubation for ~1 min, 2% uranyl acetate was added. We collected 1,600 micrographs using a FEI Tecnai F20 200 kV TEM equipped with a Gatan US4000 CCD (model 984), at a nominal magnification of ×90,000 with a digital pixel size of 6.19 Å. All image analysis was performed using Relion v3.0 on the University of Colorado Boulder High Performance Computer Cluster, Summit. Particles were manually picked from ~20 micrographs (~200 particles), which were used to generate a low-resolution 2D class average. Using these 2D averages as a starting point, we then used an iterative process to autopick particles that were used to generate our final 2D averages, and for 3D model building (in total, 42,611 particles were used to calculate the final averages shown in Fig. 1d).

**Calculation of ionic strength.** We calculated the ionic strength of our buffers as previously described<sup>64</sup>. In brief, we empirically determined the amount of KOH required for 30 mM HEPES buffer at a pH of 7.2. We estimated the proportion of protonated to unprotonated HEPES at pH 7.2 using the Henderson–Hasselbalch equation. Using the formulation for ionic strength ( $I = 1/2 \sum c_i z_i^2$ ), where  $c_i$  is the concentration, and  $z_i$  is the valence of ion type  $i$ , we determined that the ionic strength of the 50 mM potassium acetate motility buffer was 61.5 mM, the

100 mM potassium acetate and KCl buffers were 111.5 mM, and the 150 mM potassium acetate and KCl buffers were 161.5 mM. Note that we did not include the proportion of zwitterionic HEPES species (20 mM) in the calculation of ionic strength as it has been previously demonstrated to have no effect on the ionic strength of a solution, despite contributing to electrostatic interactions<sup>65</sup>.

**Dynein–Pac1 binding experiments.** Purified, gel filtered Pac1–Flag–SNAP (0.5–0.75 µg per binding experiment) was bound to Flag M2 magnetic beads (Sigma-Aldrich) by incubation in TEV buffer supplemented with 0.005% Triton X-100, 1 mM DTT and 0.1 mM Mg-ATP at 4°C. After 1 h, unbound Pac1–Flag–SNAP was removed by washing the beads four times with the same buffer. Subsequently, roughly equal amounts of purified dynein proteins (wild type, mutant, or truncation) were incubated with Pac1–Flag–SNAP-decorated beads (diluted in same buffer; the reaction volume ranged from 50–120 µl among replicates). After 1 h, the unbound fraction was removed by pipetting, whereas the bound fraction was eluted with 0.25 mg ml<sup>-1</sup> 3×Flag peptide (Sigma-Aldrich) by incubation for 20 min on ice. Bound and unbound fractions were resolved using SDS–PAGE, and the normalized, relative bound and unbound fractions were determined by measuring background-corrected band intensities. Note that we observed no binding of dynein to Flag M2 magnetic beads in the absence of Pac1–Flag–SNAP (not shown).

**Microtubule copelleting experiments.** To perform the microtubule copelleting assay, 1 µM microtubules were incubated for 10 min at room temperature with 2 nM of either wild-type or mutant dynein in motility buffer supplemented with 0.1 mg ml<sup>-1</sup> bovine serum albumin (Bio-Rad, 5000206) with or without 1 mM Mg-ATP. The reactions were subsequently pelleted using centrifugation at 21,130g for 20 min. The supernatant and pellet were separated, resuspended in sample buffer, and run on a 4–15% gradient acrylamide gel. Gels were stained with Sypro Ruby, and then imaged using a Typhoon gel imaging system (FLA 9500).

**Live-cell imaging experiments.** For the spindle dynamics assay, cells were arrested with hydroxyurea for 2.5 h, and then mounted onto agarose pads containing hydroxyurea for fluorescence microscopy<sup>32</sup>. Full Z-stacks (15 planes with 0.2 µm spacing) of GFP-labelled microtubules (GFP–Tub1) were acquired every 10 s for 9.66 min (58 time points) on a stage that was prewarmed to 30°C. To eliminate any dynein-independent contributions to spindle movements, these assays were performed in cells lacking Kar9, a protein that is required for an actin/myosin-mediated spindle orientation pathway<sup>45–47</sup>. To image dynein localization in live cells, cells were grown to mid-log phase in SD media supplemented with 2% glucose, and mounted onto agarose pads. Images were collected using a Nikon Ti-E microscope equipped with a ×100/1.49 NA TIRF objective, a Ti-S-E motorized stage, piezo Z-control (Physik Instrumente), an iXon DU888 cooled EM-CCD camera (Andor), a stage-top incubation system (Okolab) and a spinning-disc confocal scanner unit (CSUX1; Yokogawa) with an emission filter wheel (ET480/40m for mTurquoise2, ET525/50m for GFP, and ET632/60m for mRuby2; Chroma). Lasers (445 nm, 488 nm and 561 nm) housed in an LU-NV laser unit equipped with AOTF control (Nikon) were used to excite mTurquoise2, GFP and mRuby2, respectively. The microscope was controlled using NIS Elements (Nikon).

**Statistics and reproducibility.** All data were collected from at least two independent replicates (independent protein preparations or cell cultures for in vitro and in vivo experiments, respectively). The values from each independent replicate—which are indicated on each plot (see the diamonds on relevant plots)—showed similar results. We performed *t*-tests using GraphPad Prism. Statistical significance was determined using two-tailed Mann–Whitney *U*-tests (for single-molecule run-length values) or using unpaired two-tailed Welch's *t*-tests (for single-molecule velocity values). *Z* scores were calculated using the following formula:

$$Z = \frac{(\hat{p}_1 - \hat{p}_2)}{\hat{p}(1 - \hat{p}) \left( \frac{1}{n_1} + \frac{1}{n_2} \right)}$$

where:

$$\hat{p} = \frac{y_1 + y_2}{n_1 + n_2}$$

*Z* scores were converted to two-tailed *P* values using an online calculator.

**Reporting Summary.** Further information on research design is available in the Nature Research Reporting Summary linked to this article.

## Data availability

All of the yeast strains, datasets and raw video files that were generated during and/or analysed during the current study are available from the corresponding author upon reasonable request.

## References

62. Weissmann, F. et al. biGBac enables rapid gene assembly for the expression of large multisubunit protein complexes. *Proc. Natl Acad. Sci. USA* **113**, E2564–E2569 (2016).
63. Mahamdeh, M., Simmert, S., Luchniak, A., Schaffer, E. & Howard, J. Label-free high-speed wide-field imaging of single microtubules using interference reflection microscopy. *J. Microsc.* **272**, 60–66 (2018).
64. Thi de, C., Lakamper, S., Wessel, A. D., Kramer, S. & Schmidt, C. F. A chimeric kinesin-1 head/kinesin-5 tail motor switches between diffusive and processive motility. *Biophys. J.* **104**, 432–441 (2013).
65. Stellwagen, E., Prantner, J. D. & Stellwagen, N. C. Do zwitterions contribute to the ionic strength of a solution? *Anal. Biochem.* **373**, 407–409 (2008).
66. Fraley, C. & Raftery, A. E. Bayesian regularization for normal mixture estimation and model-based clustering. *J. Classif.* **24**, 155–181 (2007).
67. Redwine, W. B. et al. Structural basis for microtubule binding and release by dynein. *Science* **337**, 1532–1536 (2012).
68. Alushin, G. M. et al. High-resolution microtubule structures reveal the structural transitions in  $\alpha\beta$ -tubulin upon GTP hydrolysis. *Cell* **157**, 1117–1129 (2014).
69. Imai, H. et al. Direct observation shows superposition and large scale flexibility within cytoplasmic dynein motors moving along microtubules. *Nat. Commun.* **6**, 8179 (2015).
70. Can, S., Lacey, S., Gur, M., Carter, A. P. & Yildiz, A. Directionality of dynein is controlled by the angle and length of its stalk. *Nature* **566**, 407–410 (2019).

## Acknowledgements

We thank S. Reck-Peterson for the 8His-ZZ-Pac1-SNAP-expressing yeast strain, and members of the Markus and DeLuca laboratories for discussions. Electron microscopy

was performed at the University of Colorado, Boulder EM Services Core Facility in the MCDB Department, with the technical assistance of facility staff. This work utilized the RMACC Summit supercomputer, which is supported by the National Science Foundation (awards ACI-1532235 and ACI-1532236), the University of Colorado Boulder and Colorado State University. The RMACC Summit supercomputer is a joint effort of the University of Colorado Boulder and Colorado State University. We also thank E. Osborne-Nishimura, D. King and S. Bowerman for their assistance with using software on Summit. This research was funded by the NIH/NIGMS (GM118492, to S.M.M.).

## Author contributions

M.G.M. and S.M.M. designed the study. M.G.M. performed and analysed most of the assays, with support from S.M.M. and J.M.G. Electron microscopy was performed by Garry Morgan at the University of Colorado Boulder Electron Microscopy facility. Single-particle analysis was performed by S.M.M. with assistance from the EM facility. Reagents were generated by S.M.M., M.G.M. and J.M.G.

## Competing interests

The authors declare no competing interests.

## Additional information

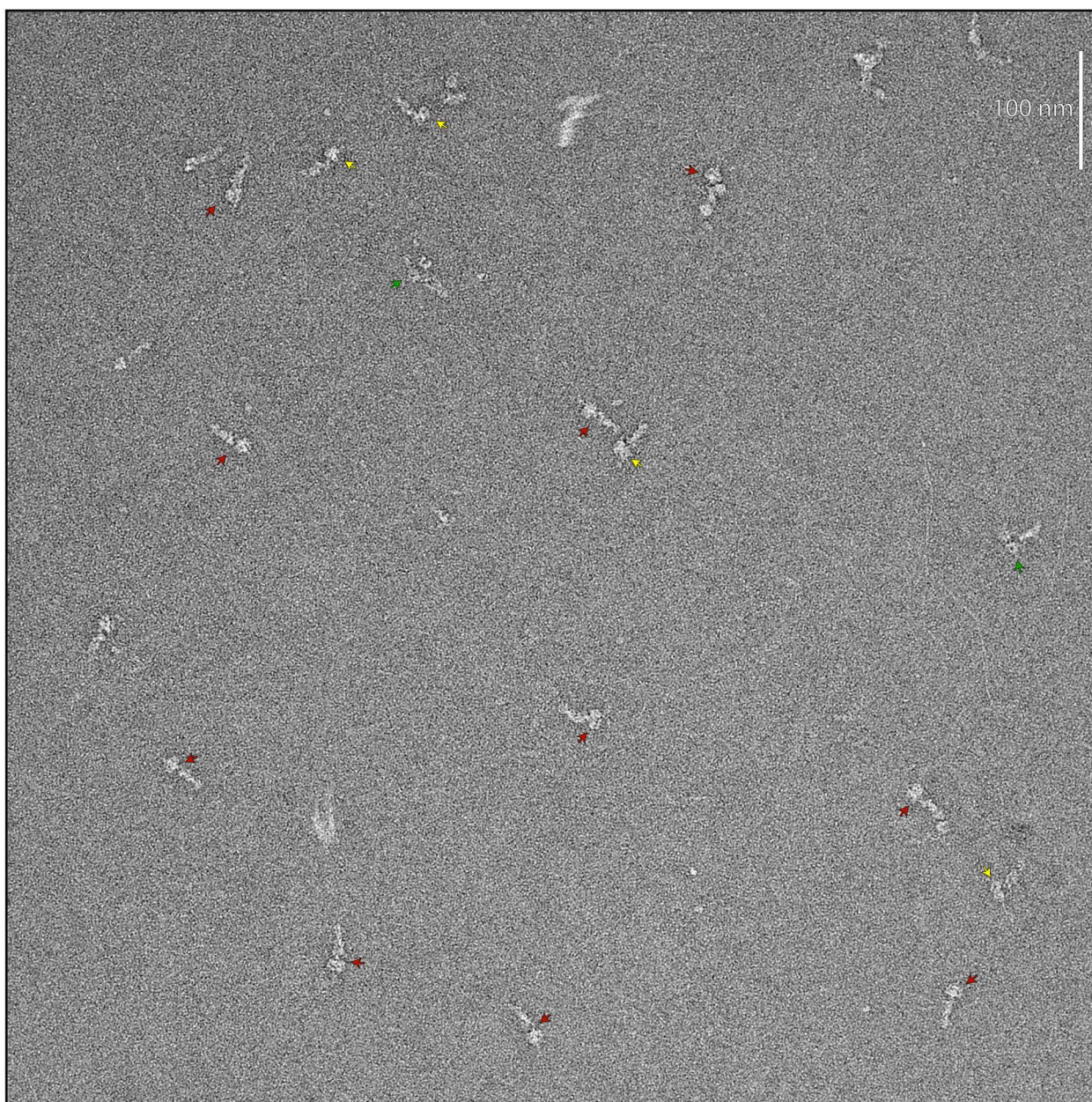
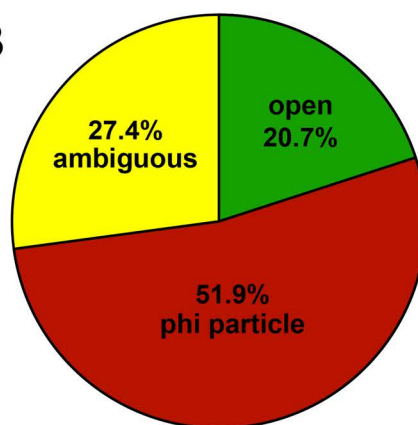
**Extended data** is available for this paper at <https://doi.org/10.1038/s41556-020-0492-1>.

**Supplementary information** is available for this paper at <https://doi.org/10.1038/s41556-020-0492-1>.

**Correspondence and requests for materials** should be addressed to S.M.M.

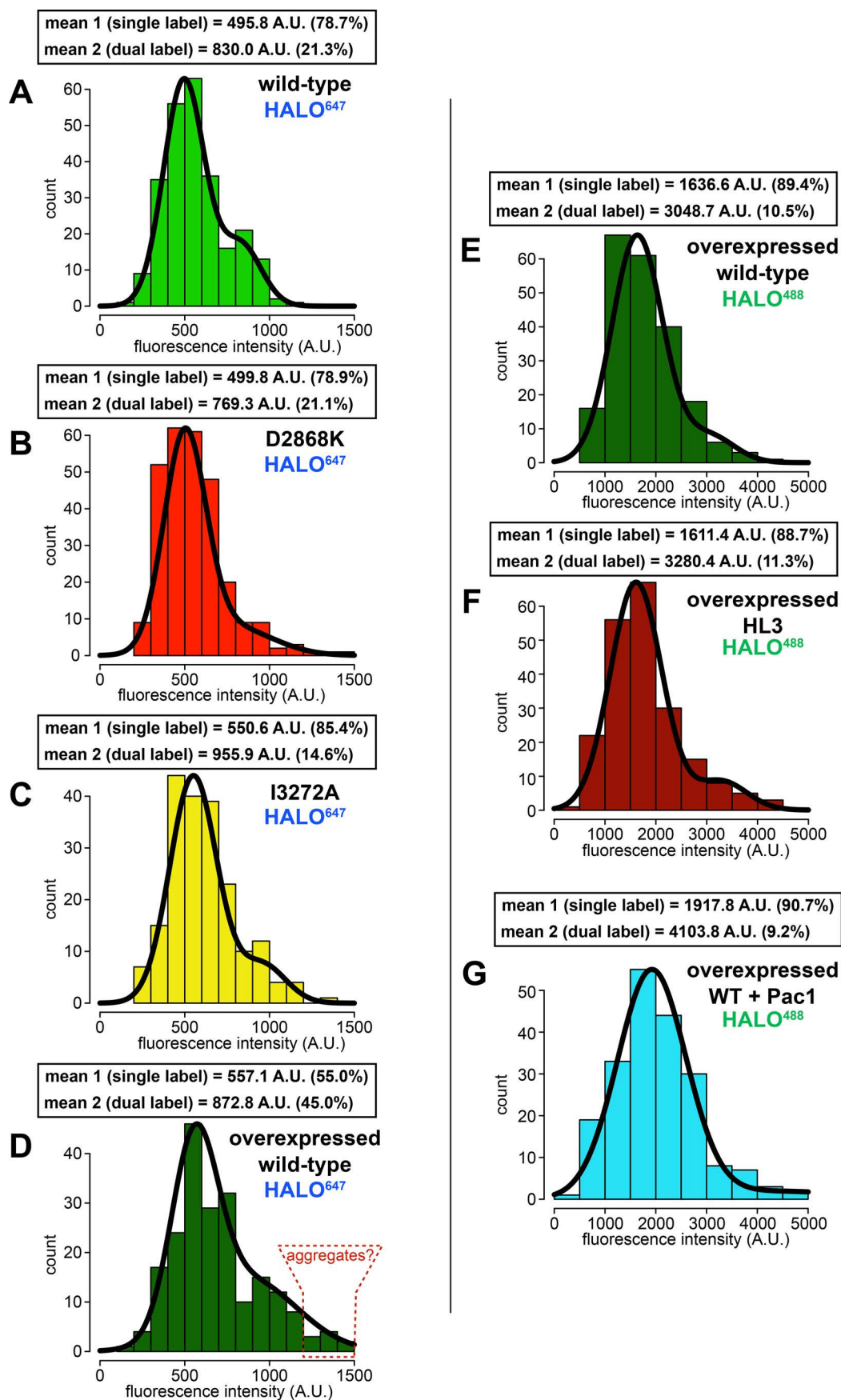
**Reprints and permissions information** is available at [www.nature.com/reprints](http://www.nature.com/reprints).



**A****B**

**Extended Data Fig. 1 | Representative raw EM image and quantitation of conformational states. a**, Representative EM image of negative stained yeast dynein complex (red arrow, phi particle conformation; green arrow, open, uninhibited conformation; yellow arrow, ambiguous). **b**, Quantitation of indicated conformational states from raw images ( $n = 435$  particles).

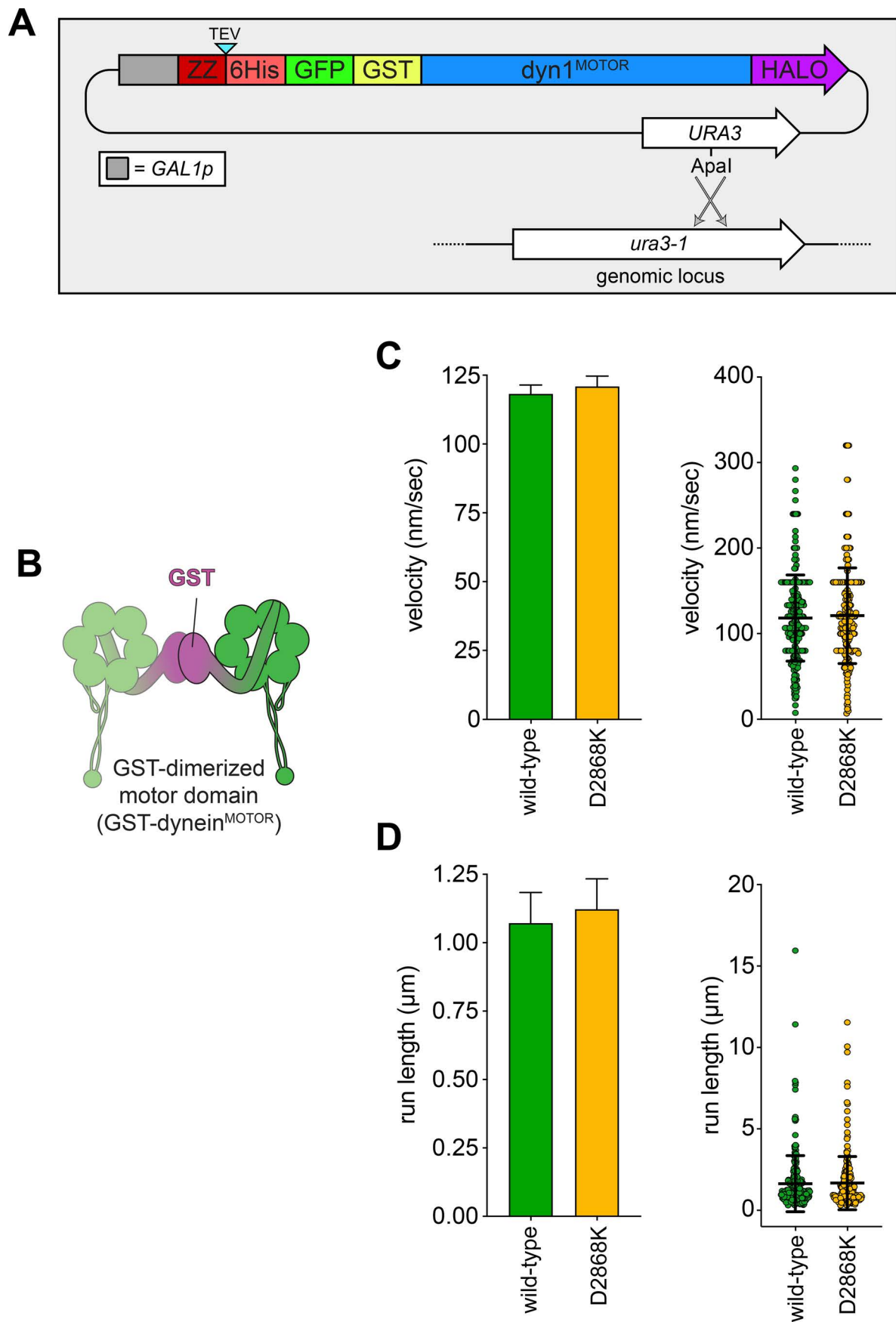




Extended Data Fig. 2 | See next page for caption.



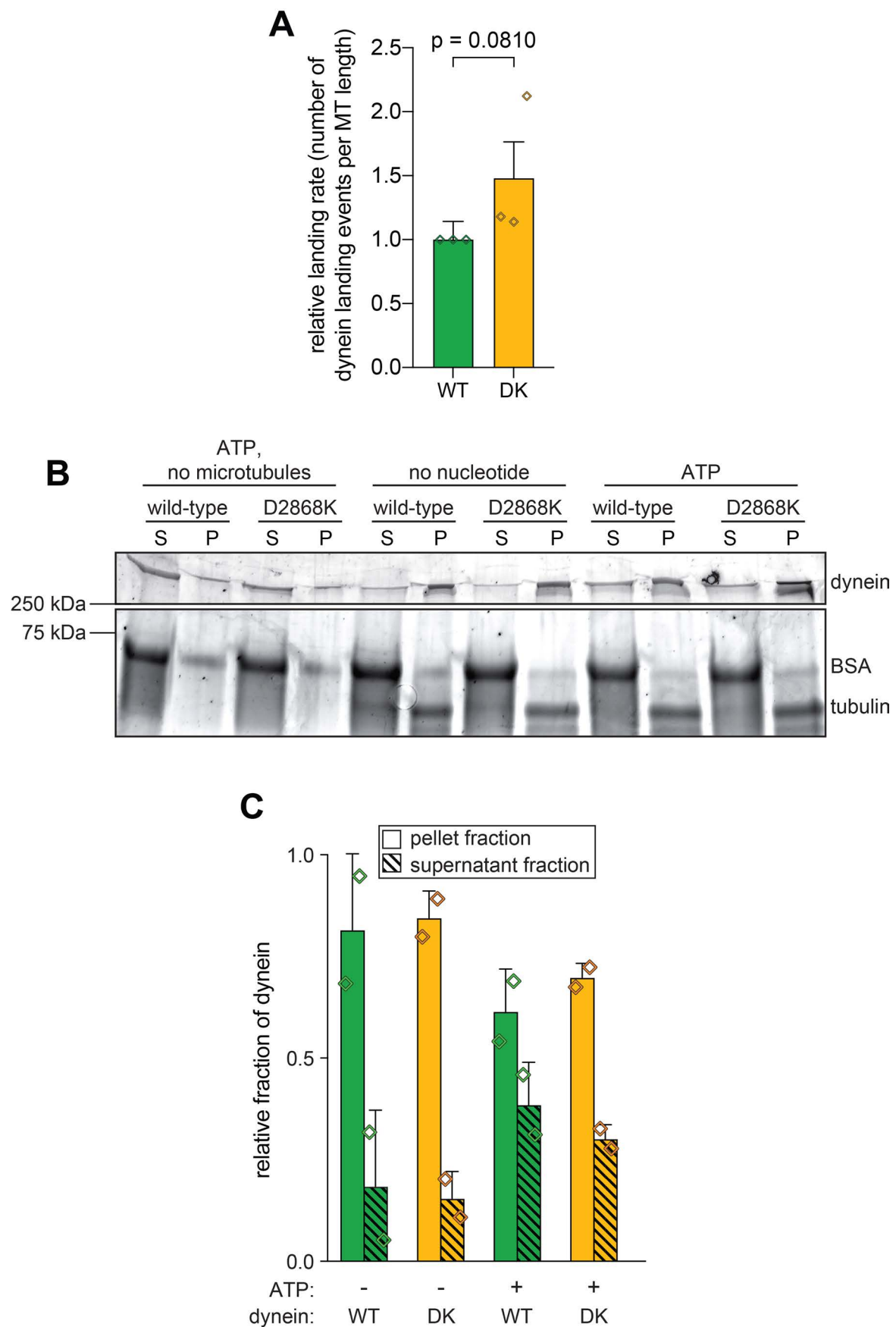
**Extended Data Fig. 2 | Fluorescence intensity analysis of native and overexpressed single molecules of dynein.** Histogram of fluorescence intensity values for single molecules of motile dyneins, as indicated, along with accompanying Gaussian fits and modeled parameters (determined using the model-based clustering algorithm Mclust<sup>66</sup>). The percentages reflect the relative proportion of molecules that fall within each component (*i.e.*, for mean 1, and mean 2). The two mean values for each likely represent single-labeled (mean 1) and dual-labeled (mean 2) dynein dimers, respectively. Red outlined region in panel D (“aggregates”), delineate particles with ~3-fold higher fluorescence intensity values than the single labeled complexes.



Extended Data Fig. 3 | See next page for caption.

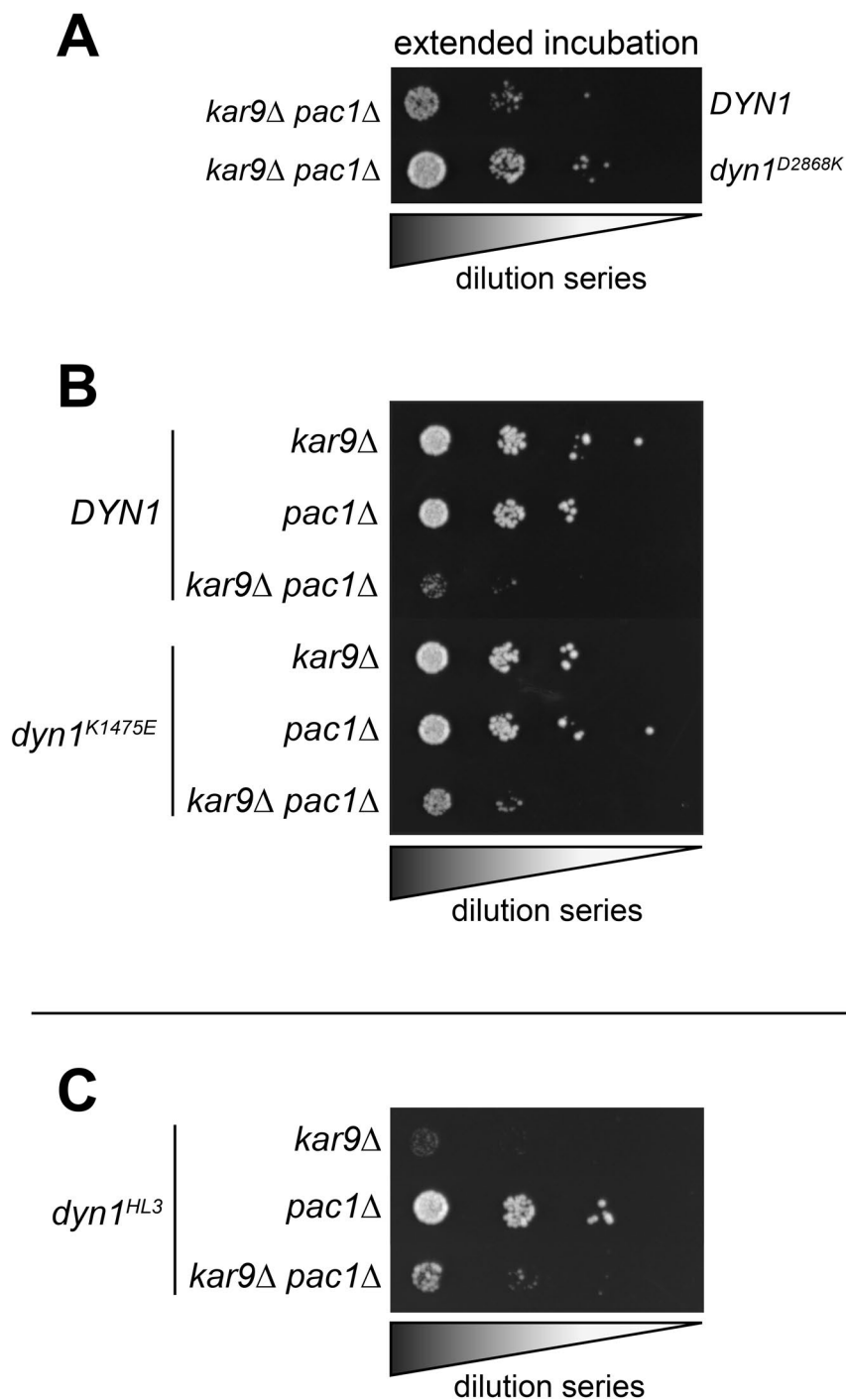
**Extended Data Fig. 3 | D2868K mutation has no effect on GST-dynein<sup>MOTOR</sup> motility.** **a**, Schematic of the plasmid used to produce GST-dynein<sup>MOTOR</sup> (wild-type and D2868K mutant). Restriction digest with Apal (cuts within *URA3* gene) targets the plasmid for homologous recombination into the *ura3-1* locus as depicted. **b**, Cartoon representation of the minimal GST-dimerized dynein motor domain (amino acids 1219-4092 of the dynein heavy chain, Dyn1). (**c** and **d**) Plots depicting mean values (left) and all values (right) for velocity (**c**) and run length (**d**) of wild-type and D2868K GST-dynein<sup>MOTOR</sup>, along with the standard error (n = 217 and 238 motors for each).



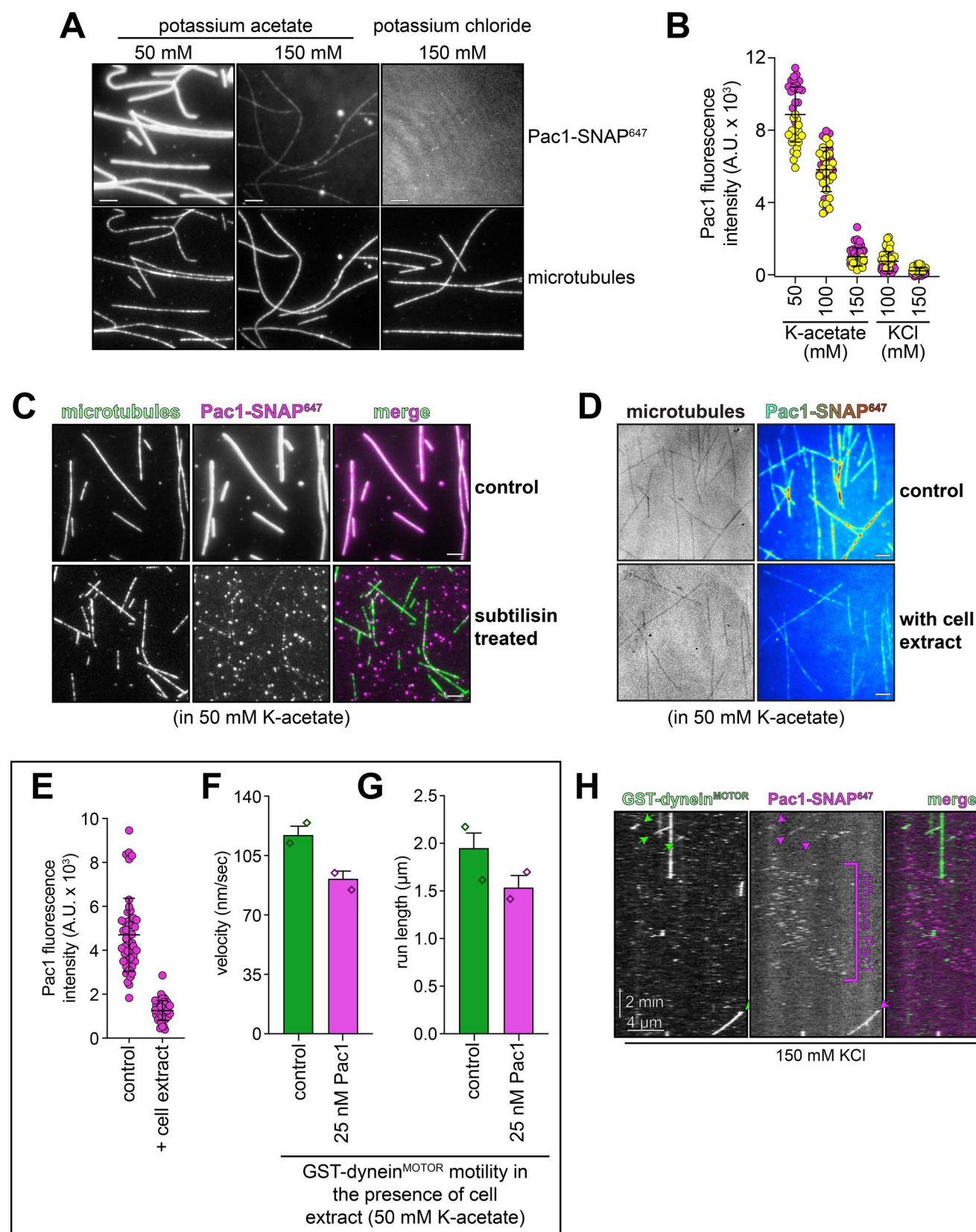


Extended Data Fig. 4 | See next page for caption.

**Extended Data Fig. 4 | Uninhibited dynein mutant exhibits only moderate increase in microtubule landing activity.** **a**, Plots depicting relative microtubule landing rate of full-length wild-type (WT) and D2868K (DK) dynein, as measured from single molecule motility experiments (mean  $\pm$  standard deviation;  $n = 554$  wild-type motors from  $1532 \mu\text{m}$  of microtubules, and  $553$  D2868K motors from  $1177 \mu\text{m}$  of microtubules; 3 independent experiments were quantitated for each). Diamonds represent mean normalized values obtained from each independent replicate experiment. Briefly, equivalent concentrations of full length wild-type or D2868K dynein were added to imaging chambers (after taking into account relative differences in labeling efficiencies, as determined from fluorescent scans of protein gels), and the number of moving motors were quantitated. Statistical significance was determined using a two-tailed Welch's  $t$  test. **(b and c)** Representative gel **(b)**; Sypro Ruby-stained) and quantitation **(c)** of microtubule co-sedimentation assay with full-length wild-type (WT) and D2868K (DK) dynein done in the absence and presence of ATP (mean  $\pm$  standard deviation;  $n = 2$  independent experiments; diamonds represent values obtained from each replicate). Relative microtubule binding was determined by measuring background-corrected band intensities of each, and subtracting any non-specific microtubule-independent pelleting (as determined from experiment performed in the absence of microtubules).



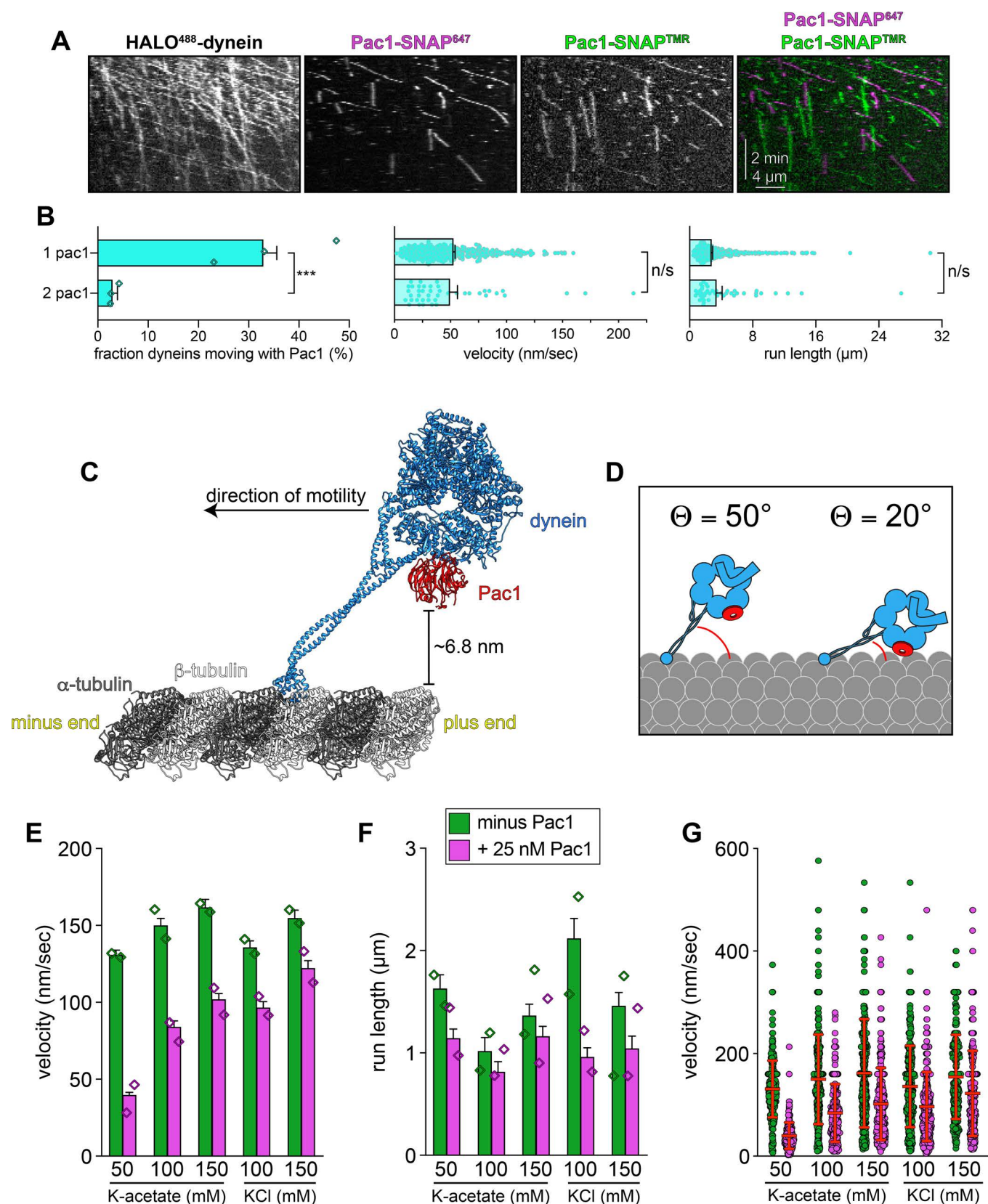
**Extended Data Fig. 5 | Synthetic interactions between dynein mutants and Kar9.** (a–c) Serial dilutions of cells with indicated genotype were plated on rich media (YPA supplemented with 2% glucose) and grown at 30 °C for 2–4 days (a, extended incubation of plates shown in Fig. 4e were grown for 4 days; all others were incubated for 2 days). Note the severe growth defects in *dyn1<sup>HL3</sup> kar9Δ* cells (in panel c), suggesting that dynein<sup>HL3</sup> is not active in cells. Note that similar results were obtained from 2 independent replicates.



Extended Data Fig. 6 | See next page for caption.



**Extended Data Fig. 6 | Pac1-microtubule binding behavior, and its contribution to dynein activity.** (**a** and **b**) Representative images (**a**) and intensity scatter plots (**b**; bars depict mean  $\pm$  standard deviation) of microtubule-bound Pac1 in different buffers. Pac1-SNAP<sup>647</sup> diluted in motility buffer (50 nM, dimer concentration) with indicated salts was introduced into a chambers with coverglass-adhered microtubules, and images were acquired (yellow and magenta circles represent data acquired from each independent experiments;  $n = 38, 49, 41, 49$ , and  $45$  microtubules that span  $911 \mu\text{m}$ ,  $1074 \mu\text{m}$ ,  $1077 \mu\text{m}$ ,  $906 \mu\text{m}$ ,  $1017 \mu\text{m}$  in length for each condition, left to right). (**c**) Pac1-microtubule binding is reduced after enzymatic removal of the unstructured tubulin carboxy-terminal tails (see Methods; similar results were obtained from 2 independent experiments). (**d–g**) Addition of cell extracts reduces Pac1-microtubule binding, and attenuates Pac1-mediated dynein velocity reduction. Representative fluorescence images of Pac1-SNAP<sup>647</sup> on microtubules (**d**; Pac1-SNAP<sup>647</sup> shown as a heat map) and scatter plots depicting intensity values (**e**; bars depict mean  $\pm$  standard deviation;  $n = 48$  and  $47$  microtubules that span  $890 \mu\text{m}$  and  $841 \mu\text{m}$  in length for each condition, left to right; similar results were obtained from 2 independent experiments). (**f** and **g**) Plots depicting the motility properties for GST-dynein<sup>MOTOR</sup> in the absence and presence of 25 nM Pac1 (dimer concentration) in low ionic strength buffer (50 mM potassium acetate) in the presence of cell extracts (0.96 mg/ml final; 275 and 258 motors, left to right, from 2 independent experiments were quantitated). Note the small Pac1-mediated GST-dynein<sup>MOTOR</sup> velocity reduction in the presence of cell extracts (22.1%, compared to 69.5% in the absence of extracts). (**h**) Additional representative kymograph of GST-dynein<sup>MOTOR</sup> comigrating with Pac1 in buffer with 150 mM KCl (see Fig. 6d and Extended Data Fig. 7E – G for quantitation and statistics). Note the diffusive behavior of Pac1 on microtubules. Scale bars in panels **a**, **c** and **d**,  $4 \mu\text{m}$ .



Extended Data Fig. 7 | See next page for caption.

**Extended Data Fig. 7 | Assessment of dynein-Pac1 stoichiometry, structural analysis of the Pac1-dynein-microtubule complex, and additional motility plots. (a and b)** Representative kymographs (**a**) and quantitation (**b**) of dynein-Pac1/2xPac1 complex motility (in motility buffer supplemented with 120 mM potassium acetate;  $n = 870$  dynein molecules from 3 independent experiments; mean values with standard error are shown, along all datapoints for middle and right plots; similar results were obtained from each replicate). Statistical significance was determined by calculating Z scores (left; \*\*\*,  $p < 0.0001$ ), using a two-tailed Mann-Whitney test (middle;  $p = 0.6068$ ), or with a two-tailed Welch's t test (right;  $p = 0.6581$ ). Note the estimated fraction of dynein-2xPac1 complexes (5.7%; see main text) is less than what would be expected if there was no cooperativity for Pac1-dynein binding (i.e., the product of the probabilities of two single, independent binding events, 10.8%). (**c and d**) Structural and cartoon model of a microtubule and Pac1-bound dynein monomer (generated with pdb 4RH7<sup>36</sup>, 3J1T<sup>67</sup>, 5VH9<sup>28</sup>, and 3J6G<sup>68</sup>). Note the close proximity of Pac1 to the microtubule surface, the latter of which is lacking the unstructured E-hooks. (**d**) Cryo-EM data reveals the dynein-microtubule angle varies due to a hinge point within the MTBD, and can be much steeper than that shown in panel A<sup>69,70</sup> ( $\Theta \geq 15-20^\circ$ , with average =  $55^\circ$ ). Cartoons depict range of angles sampled by dynein on microtubules, and thus the distances between Pac1 and the microtubule. (**e - g**) Non-normalized plots of mean values (**e and f**) and all data points (**g**; see Fig. 6d for  $n$  values) showing the relationship between Pac1-mediated dynein velocity reduction and Pac1-microtubule binding (for panels **b** left, **e**, and **f**, diamonds represent mean values obtained from each independent replicate experiment; for panel **g**, mean values and standard deviations are depicted with red lines).

## Reporting Summary

Nature Research wishes to improve the reproducibility of the work that we publish. This form provides structure for consistency and transparency in reporting. For further information on Nature Research policies, see [Authors & Referees](#) and the [Editorial Policy Checklist](#).

### Statistics

For all statistical analyses, confirm that the following items are present in the figure legend, table legend, main text, or Methods section.

n/a Confirmed

- ☐ ☒ The exact sample size ( $n$ ) for each experimental group/condition, given as a discrete number and unit of measurement
- ☐ ☒ A statement on whether measurements were taken from distinct samples or whether the same sample was measured repeatedly
- ☐ ☒ The statistical test(s) used AND whether they are one- or two-sided  
*Only common tests should be described solely by name; describe more complex techniques in the Methods section.*
- ☐ ☒ A description of all covariates tested
- ☐ ☒ A description of any assumptions or corrections, such as tests of normality and adjustment for multiple comparisons
- ☐ ☒ A full description of the statistical parameters including central tendency (e.g. means) or other basic estimates (e.g. regression coefficient) AND variation (e.g. standard deviation) or associated estimates of uncertainty (e.g. confidence intervals)
- ☐ ☒ For null hypothesis testing, the test statistic (e.g.  $F$ ,  $t$ ,  $r$ ) with confidence intervals, effect sizes, degrees of freedom and  $P$  value noted  
*Give  $P$  values as exact values whenever suitable.*
- ☒ ☐ For Bayesian analysis, information on the choice of priors and Markov chain Monte Carlo settings
- ☒ ☐ For hierarchical and complex designs, identification of the appropriate level for tests and full reporting of outcomes
- ☒ ☐ Estimates of effect sizes (e.g. Cohen's  $d$ , Pearson's  $r$ ), indicating how they were calculated

*Our web collection on [statistics for biologists](#) contains articles on many of the points above.*

### Software and code

Policy information about [availability of computer code](#)

Data collection For microscope control: NIS Elements 5.02.01

Data analysis  
For negative stain EM CTF determination: GCTFv1.06  
For negative stain EM particle classification: Relion 3.0  
For fluorescence image analysis: ImageJ v. 1.47  
For statistics and plotting: GraphPad Prism 8.2.1

For manuscripts utilizing custom algorithms or software that are central to the research but not yet described in published literature, software must be made available to editors/reviewers. We strongly encourage code deposition in a community repository (e.g. GitHub). See the Nature Research [guidelines for submitting code & software](#) for further information.

### Data

Policy information about [availability of data](#)

All manuscripts must include a [data availability statement](#). This statement should provide the following information, where applicable:

- Accession codes, unique identifiers, or web links for publicly available datasets
- A list of figures that have associated raw data
- A description of any restrictions on data availability

All yeast strains, and datasets generated during and/or analyzed during the current study are available from the corresponding author upon request. Note that we have also included source data used to generate figures.



# Field-specific reporting

Please select the one below that is the best fit for your research. If you are not sure, read the appropriate sections before making your selection.

☒ Life sciences ☐ Behavioural & social sciences ☐ Ecological, evolutionary & environmental sciences

For a reference copy of the document with all sections, see [nature.com/documents/nr-reporting-summary-flat.pdf](https://www.nature.com/documents/nr-reporting-summary-flat.pdf)

## Life sciences study design

All studies must disclose on these points even when the disclosure is negative.

Sample size	No statistical methods were used to determine sample size. Sample sizes were chosen that were sufficient to determine robust statistical differences by two-tailed Mann-Whitney , Welch's t-test, or by calculating Z score.
Data exclusions	For EM averages, particles that were not computationally assigned to classes were excluded. For single molecule motility assays, static molecules, and those with very short run lengths (< 2 pixels, or <300 nm) were excluded from velocity and run length analyses due to the ambiguous nature of the motility parameters of these molecules. These criteria were established prior to analysis.
Replication	Live cell and single molecule microscopy assays were reproduced from at least 2 independent datasets collected from samples prepared with different protein purifications, or independently prepared cell cultures. All attempts at replication were successful.
Randomization	All mutant proteins were treated and analyzed independently.
Blinding	Blinding was not possible as experimental set-up, and data-analysis were performed by the same individuals.

## Reporting for specific materials, systems and methods

We require information from authors about some types of materials, experimental systems and methods used in many studies. Here, indicate whether each material, system or method listed is relevant to your study. If you are not sure if a list item applies to your research, read the appropriate section before selecting a response.

### Materials & experimental systems

n/a	Involved in the study
<input type="checkbox"/>	<input checked="" type="checkbox"/> Antibodies
<input type="checkbox"/>	<input checked="" type="checkbox"/> Eukaryotic cell lines
<input checked="" type="checkbox"/>	<input type="checkbox"/> Palaeontology
<input checked="" type="checkbox"/>	<input type="checkbox"/> Animals and other organisms
<input checked="" type="checkbox"/>	<input type="checkbox"/> Human research participants
<input checked="" type="checkbox"/>	<input type="checkbox"/> Clinical data

### Methods

n/a	Involved in the study
<input checked="" type="checkbox"/>	<input type="checkbox"/> ChIP-seq
<input checked="" type="checkbox"/>	<input type="checkbox"/> Flow cytometry
<input checked="" type="checkbox"/>	<input type="checkbox"/> MRI-based neuroimaging

## Antibodies

Antibodies used	Commercially available anti-tubulin antibodies (Accurate chemical & scientific corporation; Cat #: YSRTMCA77G; clone YL1/2) were used to adhere microtubules to the cover glass for single molecule assays. Antibody was diluted 1:50 (to 8 µg/ml) before use. Lot number 147397 used.
Validation	Validation statement not provided by supplier. See Kilmartin, J. V., B. Wright, and C. Milstein, 1982, J. Cell Biol., 93:576-582; Wehland, J., M. C. Willingham, and I. V. Sandoval, 1983, J. Cell Biol., 97:1467-1475; and, Wehland J, and Willingham MC, 1983, J. Cell. Biol., 97; 1476-90.

## Eukaryotic cell lines

Policy information about [cell lines](#)

Cell line source(s)	ExpiSF9 cells (Life Technologies, catalog #A35243)
Authentication	Authentication by supplier.
Mycoplasma contamination	Tested negative for mycoplasma contamination by manufacturer (tested using qPCR).
Commonly misidentified lines (See <a href="#">ICLAC</a> register)	No commonly misidentified cell lines were used throughout this study.